Seismic slip on an upper plate normal fault during a large subduction megathrust rupture

Stephen P. Hicks* and Andreas Rietbrock

Liverpool Earth Observatory, University of Liverpool

Address: Jane Herdman Laboratories, 4 Brownlow Street, Liverpool, L69 3GP

Email: s.hicks@liverpool.ac.uk

Summary

Quantification of stress accumulation and release during subduction zone seismic cycles requires an understanding of the distribution of fault slip during earthquakes. Reconstructions of slip are typically constrained to a single, known fault plane. Yet, slip has been shown to occur on multiple faults within the subducting plate[1] due to stress triggering[2], resulting in phenomena such as earthquake doublets[3]. However, rapid stress triggering from the plate interface to faults in the overriding plate has not been documented. Here we analyse seismic data from the magnitude 7.1 Araucania earthquake that occurred in the Chilean subduction zone in 2011. We find that the earthquake, which was reported as a single event in global moment tensor solutions[4,5], was instead composed of two ruptures on two separate faults. Within 12 seconds, a thrust earthquake on the plate interface triggered a second large rupture on a normal fault 30 km away, in the overriding plate. This configuration of partitioned rupture is consistent with normal-faulting mechanisms in the ensuing aftershock sequence. We conclude that plate interface rupture can trigger almost instantaneous slip in the overriding plate of a subduction zone. This shallow upper plate rupture may be masked from teleseismic data, posing a challenge for real-time tsunami warning systems.

Main body

A recent succession of large (M_w > 8) earthquakes in circum-Pacific subduction zones has focussed attention on the relationship between physical properties and stress distribution along the megathrust plate interface. Seismic ruptures along the megathrust can be viewed as smooth and spatially varying patches of slip on a single fault; in this case, the subducting plate interface[6]. The fault geometry used in early coseismic slip models is underpinned by centroid moment tensor (CMT) solutions often reported by earthquake monitoring agencies. Although more sophisticated slip inversions use curved faults based on regional subduction geometry[7], slip is nearly always assigned to a single fault.

An alternative rupture configuration is slip occurring on separate faults due to static or dynamic triggering processes[2], resulting in phenomena such as doublets[3]. A doublet is the occurrence of two nearby earthquakes with similar magnitude. The time delay between ruptures can range from months[3] to seconds[1]. Many documented cases of subduction zone doublets involve triggering between the subducting plate interface and deep-rooted faults in the downgoing plate[3,8]. Although the implications for tsunami hazard are significant, there are no reported cases of rapid triggering from the plate interface to the upper plate, where there are complex faulting networks[9,10]. To resolve triggered faulting in such cases, dense local seismic observations are needed.

A region with a suitably dense network of seismometers is the central Chile subduction zone following the M_w 8.8 Maule earthquake in 2010. The ensuing aftershock sequence was captured in detail by the International Maule Aftershock Deployment[11]. Here, we focus on the largest interplate aftershock of the Maule sequence: the M_w 7.1 Araucania earthquake that occurred on 2 January 2011 at 20:20:18 UTC. Based on CMT solutions derived from teleseismic waveforms, the Araucania earthquake appears to be a ‘straightforward’ plate interface thrusting

47 event[4,5]. Its epicentre (Supplementary Note 1, Supplementary Table 1) lies in a region that acted
48 as a barrier during the 1960 M_w 9.5 Valdivia[12] and 2010 M_w 8.8. Maule[6,11] earthquakes (Fig. 1).
49 Moreover, the upper plate in this region is heavily faulted[6,10]. Therefore, the Araucania
50 earthquake is an ideal candidate to examine possible interactions between the plate interface
51 and upper plate faults.

52 We employed a multiple point-source inversion of regional seismic data[13,14]. Compared to
53 conventional slip inversions along pre-defined fault planes[6] and single point-source CMT
54 inversions[5], we can retrieve centroid times of sub-events and permit multiple faulting styles on
55 a grid of trial point-sources. A detailed understanding of 3-D crustal velocity structure[15,16]
56 ensures robust waveform inversion. Synthetic tests (Supplementary Note 2) show that we can
57 accurately resolve a range of extended source configurations involving offshore rupture using
58 the available station distribution.

59 Using the observed data, we first investigated whether low-frequency waveforms (0.02–0.04
60 Hz) in the near-field could represent the earthquake as a single point-source. The optimal
61 regional CMT solution provides a good fit to the observed waveforms at most stations
62 (Supplementary Figure 2). The centroid lies close to our relocated epicentre; its mechanism is
63 consistent with the teleseismic GCMT and USGS solutions (Fig. 1), indicating thrusting along
64 the plate interface. A high double-couple percentage (%DC) indicated by the global (98%) and
65 our regional solutions (85%) suggests a simple faulting mechanism. When we increase the
66 upper frequency limit to >0.06 Hz, waveform variance reduction (VR) sharply decreases and,
67 at the upper limit of 0.08 Hz, we notice two clear arrivals in the observed waveforms (Fig. 1b
68 & Supplementary Figure 3). Therefore, the next step is to consider whether a complex source
69 can be resolved using higher frequency waveforms and a multiple point-source
70 parameterisation.

A two-point-source model is a logical progression; an $M_w \sim 7$ earthquake likely comprises no more than two to three patches of slip[17]. Compared with that of using the first source alone (VR = 0.57), introduction of the second source significantly increases the waveform fit (Fig. 2a) by 30% (VR = 0.73), which is statistically significant to within the 99.5% confidence interval (Supplementary Note 3). Mechanisms at each trial point-source position are very consistent, with sharp correlation maxima (Fig. 2b). Based on our results, we can confidently identify the following sequence of events, which can be regarded as a closely-spaced doublet (CSD), both in time and space. Following nucleation, Event I (M_w 6.8) ruptured the megathrust beneath the coast. No more than twelve seconds later, Event II (M_w 6.7) ruptured to the southwest at a shallower depth and with an oblique normal faulting mechanism (Fig. 2).

Locations and mechanisms of aftershocks (Supplementary Note 4) that followed the Araucania earthquake support this CSD configuration. From our 44 relocated events, it is clear that there are two distinct groups of aftershocks (Fig. 3a). One group is located in the coastal region (hereafter, Group A); the other 30–40 km to the southwest (hereafter, Group B). Group B aftershocks have shallower depths, located within the marine forearc, up to 9 km above the plate interface (Fig. 3b). We obtained 19 robust CMT solutions from this aftershock sequence (Fig. 3), all of which have depths in agreement with their hypocentral location, based on a 3-D velocity model and ocean-bottom observations[15]. Normal faulting mechanisms dominate aftershock Group B. Group A aftershocks comprise mixed mechanisms, but interplate thrust faulting is most common.

A puzzling location discrepancy between Event II and aftershock Group B (Supplementary Figure 4) leads us to assess location bias in the multiple point-source inversion. So far, we have computed synthetic seismograms by calculating Green's functions in a 1-D velocity model. However, in the shallow regions of subduction zones, there are strong lateral velocity gradients (Figs. 3 & Supplementary Figure 5), particularly in S-wave velocity. Therefore, a more realistic

velocity model can improve waveform fits and make source inversions more stable. To account for lateral velocity variations, we simulated waveforms in a 3-D velocity model[15,16] using the spectral element code SPECFEM3D[18]. We used 3-D synthetics based on our two-point-source solution as input to a multiple point-source inversion using 1-D Green's functions. While the position of Event I remains stable, we find that the inversion shifts Event II 12 km to the south (from position 16 to 15; Supplementary Figure 6). Similarly, when we simulate the waveforms from Event II at the location of aftershock Group B (position 17), we find a similar southward shift, as implied from the real data inversion. Therefore, it is likely that Event II occurred ~12 km northward with respect to the formal inversion result of Fig. 2b (Supplementary Table 5). This result demonstrates the importance of 3-D structural models to obtain accurate source parameters of offshore subduction earthquakes.

Based on our aftershock analyses and 3-D waveform simulations it is now clear that Event II ruptured on a normal fault near the base of the overriding crust (Figs. 3 & 4). Group B aftershocks are located close to the prominent Mocha-Villarrica fault zone (Fig. 3). This fault may be related to strong velocity contrasts in the marine forearc beneath Isla Mocha, where Group B aftershocks are located (Figs. 3 & 4). Crustal faulting in the region is pervasive and may extend through the entire crust[10,19]; it is plausible that the geometry of fault networks becomes more complex at the base of the forearc with possible conjugate faulting (Fig. 4). We speculate that these faults are compressional during the interseismic period, but a stress inversion following the Maule earthquake[20] may favour post-seismic extension. Based on approximate fault areas from scaling relations[21], the two fault planes of Events I and II likely do not intersect. There are several possible mechanisms for the triggering of a rupture by a preceding earthquake. Dynamically triggered rupture of the normal fault is likely the dominant failure mechanism given that Event II's centroid time coincides with the passage of high-

amplitude S-wave arrivals from Event I (Supplementary Figure 7). However, we cannot completely rule out static stress transfer acting as a partial trigger.

To our knowledge, these results provide the first documented case of plate interface thrusting instantaneously activating a large rupture in the overriding plate through dynamic triggering. Past subduction zone doublets have been identified by high non-double components in their CMT solutions[8]. Conversely, in the case of the Araucania earthquake, the low-frequency single point-source solutions of both the global and regional CMT solutions did not yield a low %DC (Fig. 1). This discrepancy is also evidenced by our synthetic tests. It is possible that the short time delay and small distance between Events I and II masks rupture complexity in teleseismic CMT solutions. Therefore, CSDs may be completely hidden from global networks. CSDs may, however, be detected from a greater proportion of high frequency radiation in regional waveforms (Supplementary Note 5, Supplementary Figure 8), although this character may depend on several other source parameters, such as rupture duration. CMT solutions provided by global reporting agencies are accepted by the seismological community and form the basis of slip inversions and examinations of the stress field. CMTs are, therefore, a pillar of earthquake science, yet our results recommend their careful use in the case of slip on multiple fault planes.

The precedent set by this study also presents a new perspective for tsunami hazard assessment in subduction zones. Reverse faults as well as normal faults could theoretically be immediately triggered by megathrust slip, causing large seafloor displacement. A wide variety of upper plate faults are present in many subduction zones. For example, steeply-dipping normal faults have been imaged in the upper plate along the N. Chile and S. Peru margins[9]. Furthermore, a large upper-plate reverse faulting event preceded the 2014 M_w 8.2 Pisagua, N. Chile earthquake[22] and backthrust faults are widespread in the Sumatra subduction zone[23]. An M_w 7.0 rupture in the upper plate could result in substantial vertical seafloor displacement of 1.2 m (Supplementary

Note 6). If this scenario were scaled up to a larger rupture (M_w ~7.5), slip on the forearc fault could cause a localised tsunami on the continental shelf, although the upper limit of rupture size is controlled by the geometry and frictional properties of these faults (Fig. 3). A tsunami may be caused by static vertical displacement or through submarine landslides (Fig. 4), which have occurred locally in the past[24]. Yet without local strong-motion instruments, GPS networks, or close inspection of regional waveforms, near-field triggered ruptures will be difficult to detect. We speculate that the lack of evidence for Event II in single-source CMT solutions may result in part from the short timing between the two sources. Therefore, we recommend that the capability of teleseismic CMT inversions to resolve different doublet configurations is given a full assessment. Furthermore, there is a need to re-evaluate CMT solutions for large earthquakes using local and regional waveforms in subduction zones globally to examine whether CSDs involving the upper plate are ubiquitous.

References

1. Lay, T., Duputel, Z., Ye, L. & Kanamori, H. The December 7, 2012 Japan Trench intraplate doublet (Mw 7.2, 7.1) and interactions between near-trench intraplate thrust and normal faulting. *Phys*. *Earth*. *Planet*. *Inter*. **220,** 73–78 (2013).
2. Freed, A. M. Earthquake triggering by static, dynamic, and postseismic stress transfer. *Annu*. *Rev*. *Earth Planet*. *Sci*. **33,** 335–367 (2004).
3. Ammon, C. J., Kanamori, H. & Lay, T. A great earthquake doublet and seismic stress transfer cycle in the central Kuril islands. *Nature* **451,** 561–565 (2008).
4. United States Geological Survey National Earthquake Information Center. M7.2 - Araucania, Chile. (2011). at <http://earthquake.usgs.gov/earthquakes/eventpage/usp000hsfq#scientific_tensor>
5. Ekström, G., Nettles, M. & Dziewoński, A. M. The global CMT project 2004–2010: Centroid-moment tensors for 13,017 earthquakes. *Phys*. *Earth*. *Planet*. *Inter*. **200-201,** 1–9 (2012).
6. Moreno, M. *et al*. Toward understanding tectonic control on the Mw 8.8 2010 Maule Chile earthquake. *Earth Planet*. *Sci*. *Lett*. **321–322,** 152–165 (2012).
7. Hayes, G. P., Wald, D. J. & Johnson, R. L. Slab1. 0: A three- dimensional model of global subduction zone geometries. *J*. *Geophys*. *Res*. **117, B1** (2012).
8. Lay, T. *et al*. The 2009 Samoa-Tonga great earthquake triggered doublet. *Nature* **466,** 964–968 (2010).
9. Audin, L., Lacan, P., Tavera, H. & Bondoux, F. Upper plate deformation and seismic barrier in front of Nazca subduction zone: The Chololo Fault System and active tectonics along the Coastal Cordillera, southern Peru. *Tectonophysics* **459,** 174–185 (2008).
10. Melnick, D., Bookhagen, B., Strecker, M. R. & Echtler, H. P. Segmentation of megathrust rupture zones from fore-arc deformation patterns over hundreds to millions of years, Arauco peninsula, Chile. *J*. *Geophys*. *Res*. *Solid Earth* **114,** B01407 (2009).
11. Rietbrock, A. *et al*. Aftershock seismicity of the 2010 Maule Mw= 8.8, Chile, earthquake: Correlation between co-seismic slip models and aftershock distribution? *Geophys*. *Res*. *Lett*. **39,** L08310 (2012).
12. Moreno, M. S., Bolte, J., Klotz, J. & Melnick, D. Impact of megathrust geometry on inversion of coseismic slip from geodetic data: Application to the 1960 Chile earthquake. *Geophys*. *Res*. *Lett*. **36,** L16310 (2009).
13. Sokos, E. & Zahradnik, J. A Matlab GUI for use with ISOLA Fortran codes. *Users' guide* (2006).
14. Zahradnik, J., Serpetsidaki, A., Sokos, E. & Tselentis, G.-A. Iterative Deconvolution of Regional Waveforms and a Double-Event Interpretation of the 2003 Lefkada Earthquake, Greece. *B*. *Seismol*. *Soc*. *Am*. **95,** 159–172 (2005).
15. Hicks, S. P., Rietbrock, A., Ryder, I. M. A., Lee, C.-S. & Miller, M. Anatomy of a megathrust: The 2010 M8.8 Maule, Chile earthquake rupture zone imaged using seismic tomography. *Earth Planet*. *Sci*. *Lett*. **405,** 142–155 (2014).
16. Haberland, C., Rietbrock, A., Lange, D., Bataille, K. & Dahm, T. Structure of the seismogenic zone of the southcentral Chilean margin revealed by local earthquake

traveltime tomography. *J*. *Geophys*. *Res*. **114,** B01317 (2009).

17. Zahradnik, J. & Sokos, E. The Mw 7.1 Van, Eastern Turkey, earthquake 2011: two-point source modelling by iterative deconvolution and non-negative least squares. *Geophys*. *J*. *Int*. **196,** 522–538 (2014).
18. Komatitsch, D., Erlebacher, G., Göddeke, D. & Michéa, D. High-order finite-element seismic wave propagation modeling with MPI on a large GPU cluster. *J*. *Comput*. *Phys*. **229,** 7692–7714 (2010).
19. Hicks, S. P., Nippress, S. E. & Rietbrock, A. Sub-slab mantle anisotropy beneath south-central Chile. *Earth Planet*. *Sci*. *Lett*. **357,** 203–213 (2012).
20. Hardebeck, J. L. Coseismic and postseismic stress rotations due to great subduction zone earthquakes. *Geophys*. *Res*. *Lett*. **39,** L21313 (2012).
21. Blaser, L., Krüger, F., Ohrnberger, M. & Scherbaum, F. Scaling Relations of Earthquake Source Parameter Estimates with Special Focus on Subduction Environment. *B*. *Seismol*. *Soc*. *Am*. **100,** 2914–2926 (2010).
22. González, G. *et al*. Upper plate reverse fault reactivation and the unclamping of the megathrust during the 2014 northern Chile earthquake sequence. *Geology* G36703.1 (2015).
23. Singh, S. C. *et al*. Evidence of active backthrusting at the NE Margin of Mentawai Islands, SW Sumatra. *Geophys*. *J*. *Int*. **180,** 703–714 (2010).
24. Geersen, J., Völker, D., Behrmann, J. H., Reichert, C. & Krastel, S. Pleistocene giant slope failures offshore Arauco Peninsula, Southern Chile. *J*. *Geol*. *Soc*. *London* **168,** 1237–1248 (2011).
25. Quintero, R., Zahradnik, J. & Sokos, E. Near-regional CMT and multiple-point source solution of the September 5, 2012, Nicoya, Costa Rica Mw 7.6 (GCMT) earthquake. *J*. *S*. *Am*. *Earth Sci*. **55,** 155–165 (2014).
26. Sokos, E. & Zahradnik, J. Evaluating Centroid- Moment- Tensor Uncertainty in the New Version of ISOLA Software. *Seismol*. *Res*. *Lett*. **84,** 656–665 (2013).
27. Casarotti, E. *et al*. in *Proceedings of the 16th International Meshing Roundtable* 579–597 (Springer Berlin Heidelberg, 2008).
28. Frohlich, C. Triangle diagrams: ternary graphs to display similarity and diversity of earthquake focal mechanisms. *Phys*. *Earth*. *Planet*. *Inter*. **75,** 193–198 (1992).
29. Hayes, G. P. *et al*. Seismotectonic framework of the 2010 February 27 Mw 8.8 Maule, Chile earthquake sequence. *Geophys*. *J*. *Int*. **195,** 1034–1051 (2013).
30. Melnick, D. & Echtler, H. P. in *The Andes* 565–568 (Springer Berlin Heidelberg, 2006). doi:10.1007/978-3-540-48684-8_30

Supplementary information

Supplementary information is linked to the online version of the paper at www.nature.com/nature.

Acknowledgments

We are grateful to all field crews from partner organisations who participated in the deployment and servicing of seismic instruments used in this study. We thank Jiří Zahradník and Efthimios Sokos for their assistance in setting up the ISOLA code. S.P.H. is funded by a NERC studentship NE/J50015X/1.

Author contributions

S.P.H. carried out the single and multiple point-source inversions, as well as the moment tensor inversion and aftershock relocations. S.P.H. wrote the manuscript, interpreted the results, and generated all figures. A.R. carried out the 3-D full waveform simulations, wrote the manuscript, and interpreted the results.

Author information

The authors declare no competing financial interests.

Correspondence and requests for materials should be addressed to S.P.H (s.hicks@liverpool.ac.uk) or A.R. (a.rietbrock@liverpool.ac.uk).

Figure Captions

Fig. 1: Location and single source solution. a) Location map. Stations used for CMT inversion are labelled with station codes. Other stations are for hypocentre relocation only (Supplementary Note 1). Shading indicates rupture areas of great earthquakes in 1960[12] and 2010[6]. Inset: Regional tectonic setting. b) Double-couple percentage (%DC) and variance reduction (VR) of the single point-source versus frequency. A transition occurs at 0.057 Hz, where VR suddenly decreases because the waveforms cannot be explained by a single source alone. This change is illustrated by representative waveforms at low and high frequencies (see Supplementary Figure 2 & Supplementary Figure 3 for details).

256

Fig. 2: Two-point-source solution. a) Observed (black) and synthetic (red) waveforms for the optimum high-frequency (0.02–0.08 Hz) solution. Station names are labelled. Numbers alongside each waveform component denote VR. Blue and green shading denotes the contribution from each event. b) Waveform correlation for each event as a function of trial point-source position (numbered). The optimum time shift of Event I and II is shown. Black beach balls are solutions that lie within 90% of the optimum solution's (red beach ball) VR. The red star denotes the earthquake's epicentre. c) Resulting moment-rate function obtained using the NNLS method.

257

Fig. 3: Aftershock analysis. (a) Map and (b) cross-section showing locations and focal mechanisms of aftershocks (Groups A and B) and mainshock events (labelled EV-I and EV-II). Faulting style is classified on principal stress orientations[28] and minimum rotation angle with respect to plate interface thrust faulting[29], accounting for plate interface geometry (black line)[15,16]. We plot the revised location of Event II, based on 3-D waveform modelling. Mapped faults are shown[10,30]; MVFZ = Mocha-Villarrica fault zone. The cross-section background is from P-wave velocity tomography models[15,16]. The star denotes the hypocentre of the Araucania earthquake; the triangle shows the coastline.

258

Fig. 4: Schematic interpretation of the Araucania earthquake rupture. Plate interface thrusting (Event I) triggered a rupture along an extensional fault in the overriding plate (Event II). It is likely that two great earthquakes in 1960 and 2010 brought both faults closer to failure. As shown by ancient submarine landslide deposits in the area, a larger-scale rupture in the overriding plate has the potential to act as a tsunamigenic earthquake. Beach balls represent the focal mechanisms of both events from Fig. 3. The inset shows the interpreted structure of conjugate normal faulting with the background colour representing v_p/v_s ratio[15].

Methods

Data selection and processing

For the waveform inversion of the Araucania earthquake, we used broadband and strong-motion stations that were located onshore within an epicentral distance of 200 km from the Araucania earthquake. We only used waveforms from stations that have a high signal-to-noise ratio (> 10) in the frequency range 0.01–0.10 Hz (Supplementary Figure 9). Due to the close proximity of some stations to the earthquake, we excluded waveform records that were either clipped, had long period disturbances, or instrument tilt effects. These quality-control checks resulted in a set of seven stations (including two strong-motion stations) located north and east of the Araucania earthquake (Fig. 1a).

Source inversion algorithm

Iterative deconvolution (ID)[14] is used for the multiple point-source inversion of deviatoric moment tensors. ID works by inverting for the optimum focal mechanism and timing of sources for a prescribed set of points to minimise the L2 misfit between observed and synthetic waveforms. A grid search is then performed to select the source position that produces the highest correlation between observed and synthetic waveforms. The first inversion explains the full waveforms using a single source, the synthetics of which are then subtracted from the observed waveforms. The remaining waveforms are then used to invert for subsequent sub-events[14]. After the retrieval of each sub-event, VR is calculated and manually assessed to ensure that additional sub-events are required by the data and the waveforms are not just fitting correlated noise. For moment tensor inversion, we use the software package, ISOLA[13], which can be accessed athttp://seismo.geology.upatras.gr/isola/. In the inversion, the moment-rate of the source is prescribed; it is found by manually searching for the source length that produces the maximum VR. If the moment-rate of the source is shorter than the minimum inverted period,

285 then the source can be represented by a delta function. To negate artifacts produced by the ID
286 method, we also test the stability of our multiple point-source solution using a non-negative
287 least squares (hereafter, NNLS) inversion method[17]. In the NNLS approach, the double-couple
288 focal mechanism at each source is prescribed. At each trial point-source position, the moment
289 rate is represented by a set of shifted triangles. The weight of each triangle is then inverted for
290 using NNLS. In this paper, we use one-second triangle shifts. The moment of each source can
291 be constrained, which stabilises the inversion, although the exact value of total moment does
292 not dramatically influence source timings or positions[25].

293 The inversion is performed on bandpass-filtered displacement waveforms. The effect of
294 different 1-D velocity models was tested; the final solutions were calculated using a velocity
295 model appropriate for the coastline of south-central Chile (Supplementary Figure 10). We
296 analysed the effect of data errors and imperfect Green's functions by systematically removing
297 pieces of data from the inversion (jackknifing). Where subsurface structure is complex, removal
298 of certain stations may have a large effect on the final solution[26]. Based on the analysis of signal
299 to noise ratio (Supplementary Figure 9), we used a lowermost frequency limit of 0.02 Hz
300 throughout this paper. The upper frequency limit was dependent on the source parameterisation
301 used (single or multiple source).

302 **Single point-source inversion strategy**

303 Guided by preliminary inversions and the anticipated fault size[21], we used a trial point-source
304 grid with a spacing of 12 km in the down-dip and along-strike directions (Fig. 2b). At this stage,
305 we wanted to resolve the simplest possible source, so the maximum frequency was kept well
306 below the corner frequency (approximately 0.1 Hz for an $M_w \sim 7$ earthquake). Therefore, we
307 chose an upper frequency limit of 0.04 Hz and assumed a delta moment-rate function. We tested
308 the robustness of the solution by jackknifing stations and their individual components. The

source position changes slightly when varying the dataset, but by no more than 17 km (Supplementary Figure 2); the largest shifts occur if the closest stations are removed from the inversion. The zone of maximum correlation is not particularly sharp, corresponding to the possible source locations from the jackknifing analysis (Supplementary Figure 2). These tests show that the source location is reasonably stable and its mechanism is consistent throughout.

We also find that as the upper frequency bandpass cut-off increases, %DC gradually decreases. This trend continues until around 0.057 Hz, above which, the full waveforms can only be explained using Events I and II, and %DC becomes very high (Fig. 1b).

Multiple point-source inversion strategy

We first carried out a multiple point-source inversion using ID, in which the deviatoric moment tensor mechanisms of both sources were allowed to vary. The grid of point-sources was kept the same as for the single point-source inversion. For the source-time function, we found that with increasing length of the triangle, the total moment gradually increases, while VR and %DC of each source reaches a maximum at 18 s (Supplementary Figure 11). We therefore fixed the triangle length of each source to 18 s for the ID multiple point-source inversion, although the point-source mechanisms remain consistent for different triangle lengths, suggesting a stable solution.

We used the NNLS method to test the robustness of the solution obtained by ID. To search for the best-fitting source configurations, we performed two inversions: one in which total moment was constrained by the ID solution; the other in which moment was allowed to vary. We tested a number of source positions and faulting styles for Events I and II using the NNLS method, but we found that the highest VR came from the two-point-source configuration found using the ID method. Using the mechanisms given by the ID solution, we then performed a grid-search over all possible combinations of the two-point-source locations using the NNLS

method. As expected, the moment-constrained inversion is most similar to the ID solution (Supplementary Figure 12). Nevertheless, both inversions produce results consistent with the ID solution. Importantly, the resulting source-time function obtained by NNLS shows that both events have a similar time function to the 18 s triangle source used in ID (Fig. 2c). In summary, we find no bias in the results caused by the inversion method.

As a further test of solution stability, we perform jackknifing tests by removing one station at a time from the inversion. The results of these tests are shown in Supplementary Table 6 and demonstrate remarkably consistent centroid positions and focal mechanisms for Events I and II. The jackknifing test therefore indicates that the optimum multiple point-source solution is not dependent on one single waveform. Furthermore, a three-point-source approximation did not meaningfully improve the waveform fit (VR = 0.76; 3% increase in VR compared with two-point-sources).

Since the ID method inverts for the first point-source before subsequently calculating the second source, we carried out a test to determine whether Event II is dependent on the chosen location and mechanism of Event I. Normally, we accept the source position that produces the highest waveform correlation. However, for this test, we fixed the position of Event I and chose the corresponding best-fitting mechanism. We carried out this test at all trial point-sources adjacent to Position 33 (the optimum position of Event I). The results of this test are shown in Supplementary Table 7. For all but one position of Event I, the position, timing, and mechanism of Event II remain consistent with the optimum solution. When Event I is fixed to Position 25, the MT solution of Event II appears less stable. However, Position 25 is directly adjacent to Position 16 (the optimum location of Event II from ID; Fig. 2b), so this discrepancy is expected because the inversion tries to explain both events at this position with a single source. In summary, we find that the Event II solution is stable with respect to the exact position and mechanism of Event I.

Mesh design for the 3-D waveform simulation

For the wave propagation simulations, we constructed a hexahedral unstructured mesh using the GEOCUBIT software package[27]. The lateral resolution at the surface is 5 km, coarsening at a refinement layer (45 km depth, which is an average Moho depth for the region[15,16]). The mesh honours surface relief and bathymetry to ensure that topographic effects on waveform propagation are accurately simulated. Our mesh does not contain dipping geological discontinuities in the subsurface, such as the oceanic Moho, due to the lack of constraints on its geometry. This mesh has been designed for simulations that are accurate up to ~0.3 Hz, well above the maximum frequency of our waveform inversions, ensuring numerically stable simulations. The Mesh used is shown in Supplementary Figure 13.

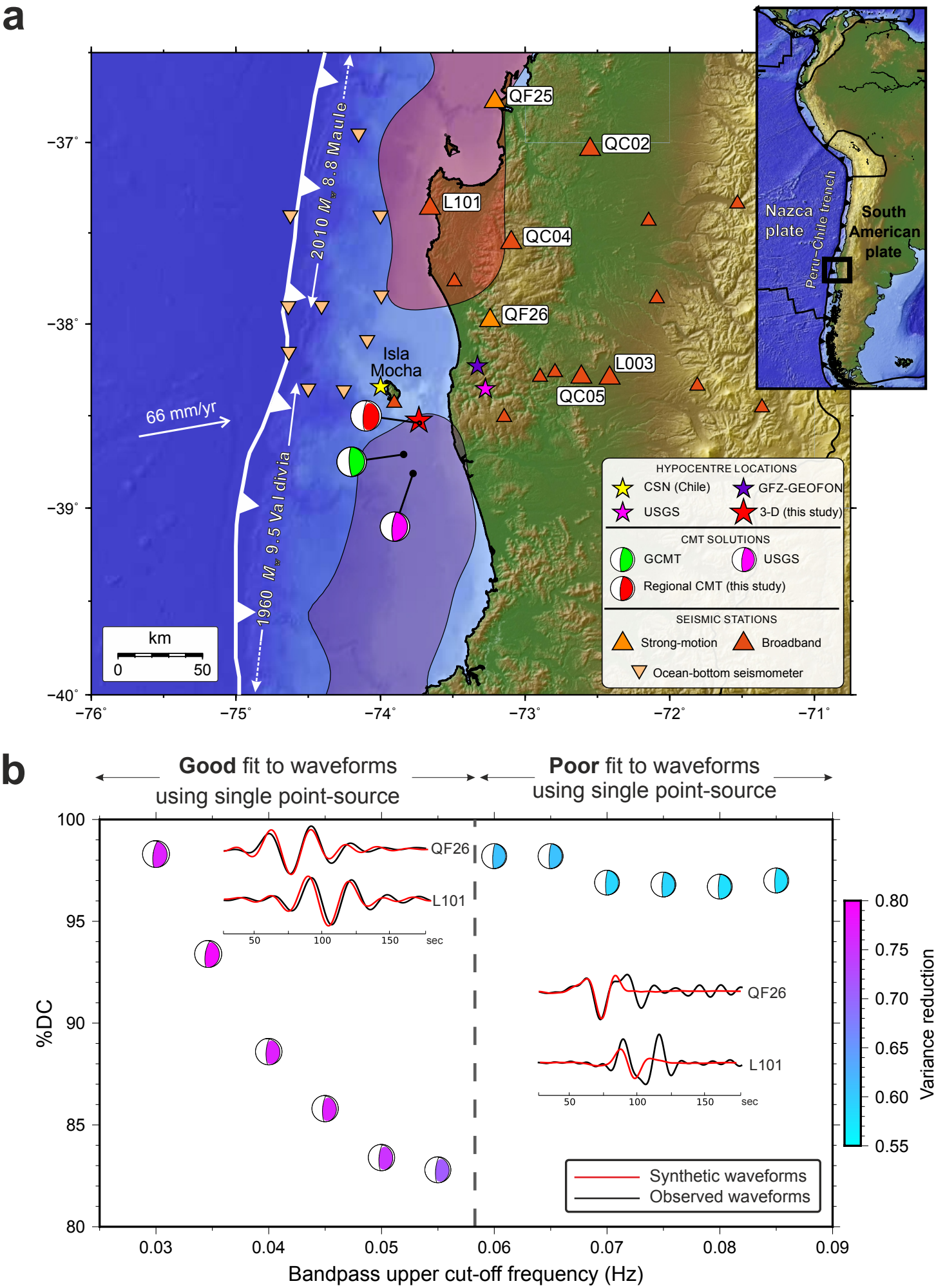
a
QF25
QC02
L101
QC04
QF26
L003
QC05
Isla Mocha
66 mm/yr
2010 M$_w$ 8.8 Maule
1960 M$_w$ 9.5 Valdivia
km
0
50
−37°
−38°
−39°
−40°
−76°
−75°
−74°
−73°
−72°
−71°
Nazca plate
South American plate
Peru–Chile trench
HYPOCENTRE LOCATIONS
CSN (Chile)
GFZ-GEOFON
USGS
3-D (this study)
CMT SOLUTIONS
GCMT
USGS
Regional CMT (this study)
SEISMIC STATIONS
Strong-motion
Broadband
Ocean-bottom seismometer
b
Good fit to waveforms using single point-source
Poor fit to waveforms using single point-source
QF26
L101
50
100
150
sec
%DC
100
95
90
85
80
0.03
0.04
0.05
0.06
0.07
0.08
0.09
Bandpass upper cut-off frequency (Hz)
Variance reduction
0.80
0.75
0.70
0.65
0.60
0.55
Synthetic waveforms
Observed waveforms

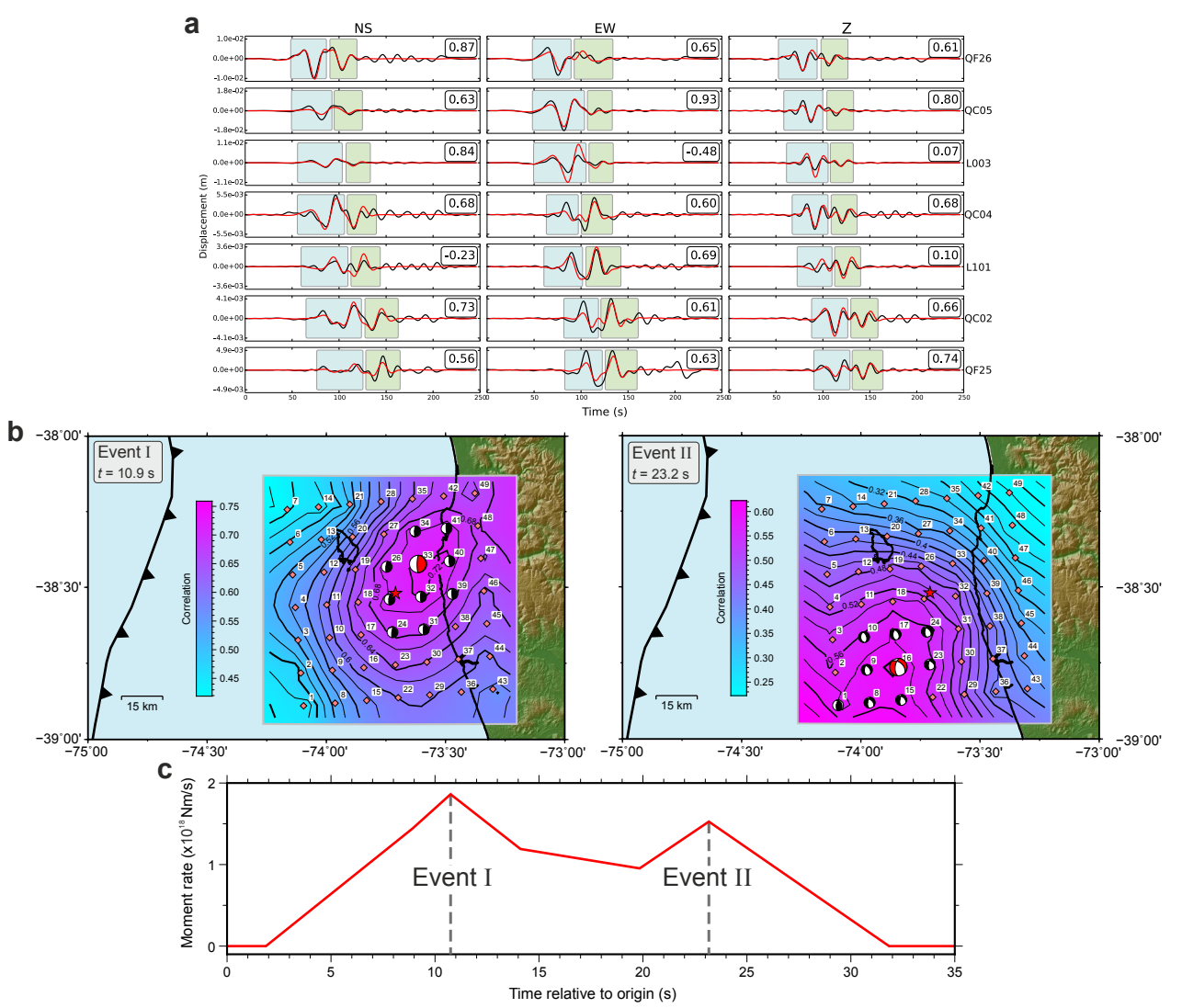
a
NS
EW
Z
0.87
0.65
0.61
QF26
0.63
0.93
0.80
QC05
0.84
-0.48
0.07
L003
0.68
0.60
0.68
QC04
-0.23
0.69
0.10
L101
0.73
0.61
0.66
QC02
0.56
0.63
0.74
QF25
Displacement (m)
Time (s)
b
Event I
t = 10.9 s
Event II
t = 23.2 s
Correlation
15 km
−38°00'
−38°30'
−39°00'
−75°00
−74°30'
−74°00'
−73°30'
−73°00'
c
Event I
Event II
Moment rate (x10^18 Nm/s)
Time relative to origin (s)

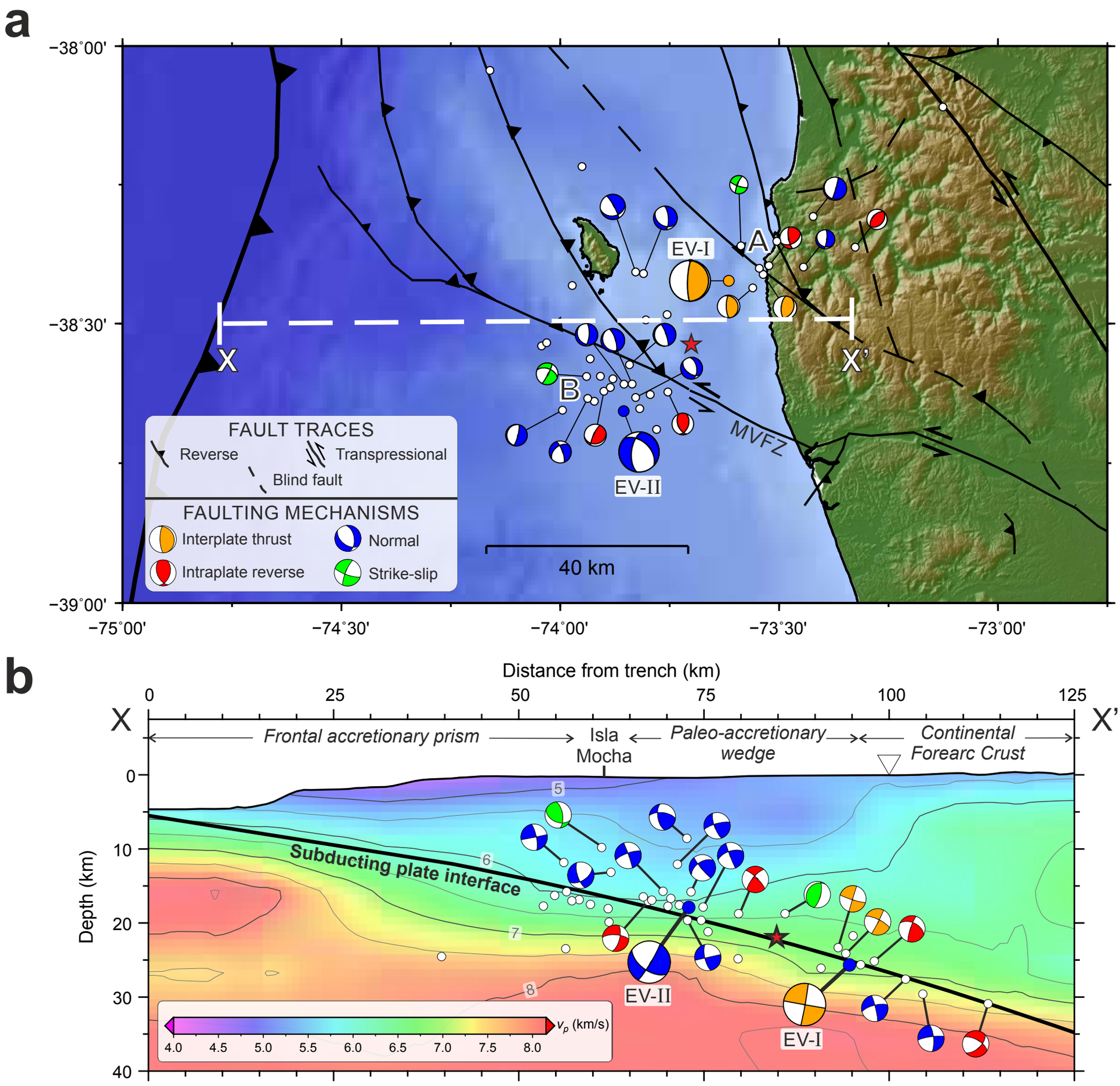
a
−38°00'
−38°30'
−39°00'
−75°00'
−74°30'
−74°00'
−73°30'
−73°00'
X
X'
A
B
EV-I
EV-II
MVFZ
40 km
FAULT TRACES
Reverse
Transpressional
Blind fault
FAULTING MECHANISMS
Interplate thrust
Normal
Intraplate reverse
Strike-slip
b
Distance from trench (km)
0
25
50
75
100
125
X
X'
Frontal accretionary prism
Isla Mocha
Paleo-accretionary wedge
Continental Forearc Crust
Depth (km)
0
10
20
30
40
5
6
7
8
Subducting plate interface
EV-II
EV-I
v_p (km/s)
4.0
4.5
5.0
5.5
6.0
6.5
7.0
7.5
8.0

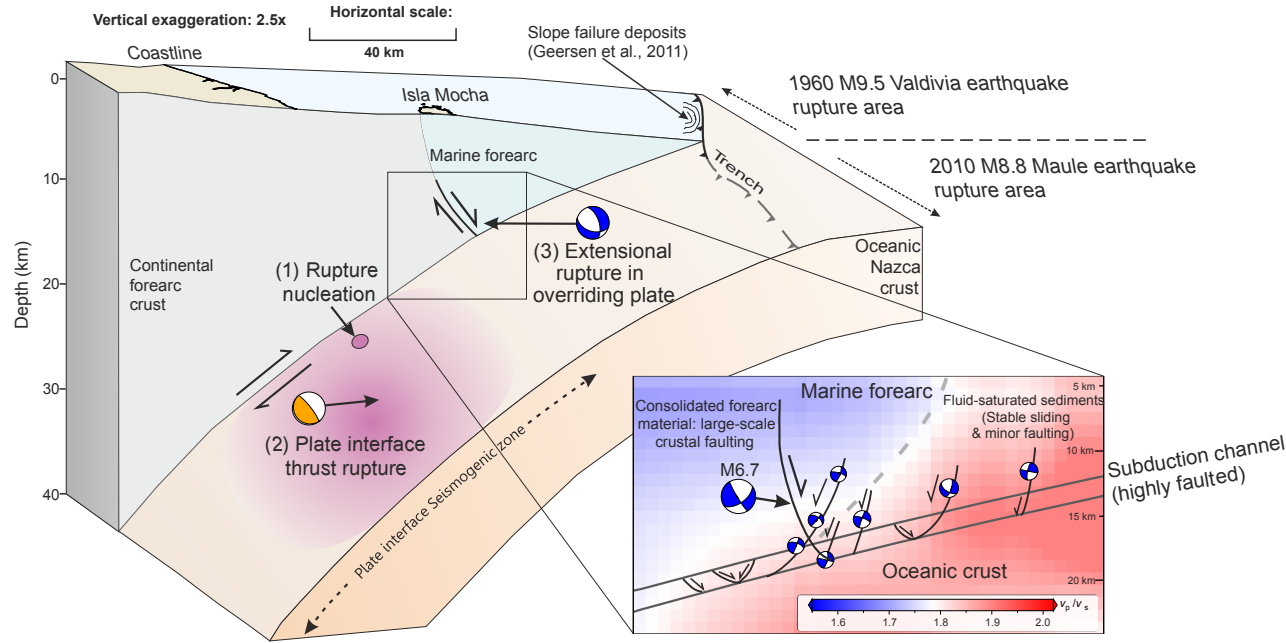
Vertical exaggeration: 2.5x
Horizontal scale:
40 km
Coastline
Slope failure deposits
(Geersen et al., 2011)
1960 M9.5 Valdivia earthquake
rupture area
2010 M8.8 Maule earthquake
rupture area
Isla Mocha
Marine forearc
Trench
Depth (km)
0
10
20
30
40
Continental
forearc
crust
(1) Rupture
nucleation
(3) Extensional
rupture in
overriding plate
Oceanic
Nazca
crust
(2) Plate interface
thrust rupture
Plate interface Seismogenic zone
Marine forearc
Consolidated forearc
material: large-scale
crustal faulting
Fluid-saturated sediments
(Stable sliding
& minor faulting)
M6.7
Subduction channel
(highly faulted)
Oceanic crust
5 km
10 km
15 km
20 km
1.6
1.7
1.8
1.9
2.0
V_p/V_s

Seismic slip on an upper plate normal fault during a large subduction megathrust rupture

Stephen P. Hicks* and Andreas Rietbrock

SUPPLEMENTARY INFORMATION

Supplementary Notes

Supplementary Note 1: Mainshock hypocentre relocation

We manually picked P- and S-wave onset times at both onshore and offshore stations at < 150 km distance (Fig. 1). The onset times were then inverted for the hypocentral location inside a local 3-D velocity model[1]. Our relocated hypocentre lies approximately halfway between the coastline and Isla Mocha, ~30 km to the north of the USGS centroid and gCMT solutions (Fig. 1, Supplementary Table 1). The hypocentral depth of 23 km is consistent with the location of the subducting plate interface, based on regional estimates of slab geometry[2,3]. The large discrepancy in the CSN (Centro Sismológico Nacional) location (30 km relative to our 3-D relocation) is due to 3-D seismic velocity variations that cannot be accounted for with a 1-D velocity model using onshore stations only. This 1-D mislocation is also demonstrated by our own relocation inside using a 1-D velocity model (Supplementary Figure 10).

Supplementary Note 2: Synthetic Sensitivity Tests

Resolving capability of multiple point-sources

Before inverting the real data, we tested the performance of our inversion strategy, and its ability to resolve multiple point-sources by simulating several different source configurations. We then inverted these synthetic waveforms as both single and multiple point-source models. Here, we describe the results using the iterative deconvolution (ID) method only. Based on global CMT solutions (Fig. 1), we assumed that the causative fault plane was the shallow, eastward dipping subducting plate interface. We designed a 2-D grid of 49 trial point-sources that lie in the same orientation as the megathrust fault (Supplementary Figure 1), according to regional plate interface geometry[1,3]. The plane of trial grid positions passes through the hypocentre of the Araucania earthquake.

Seismic slip on an upper plate normal fault during a large subduction megathrust rupture

Due to the Araucania earthquake occurring at the southernmost limit of the 2010 Maule rupture, station distribution is not ideal (Fig. 1). Therefore, it is important to consider whether station coverage impacts our ability to resolve complex sources. For this test, we calculated synthetic waveforms from configurations of two-point-sources. The two sources are separated in space and time by 40 km and 10 s, respectively. We prescribed the source-time function for each as a 15 s triangle. The second sub-event is located up-dip and to the southwest of the first sub-event, and has an extensional mechanism. The moment ratio of both subevents (M_{o1}/M_{o2}) is kept fixed at 1.5. We choose this configuration since it represents the most extreme scenario where both sub-events have different mechanisms and where the second, weaker sub-event is located furthest away from, and in the opposite direction to, the network. From our results, there is a straightforward and encouraging conclusion. Although the azimuthal coverage provided by the seismic network is limited, the multiple point-source inversion performs well and it is able to resolve source complexity in this extreme scenario. In fact, using only two stations can retrieve both sources reasonably well, provided these stations cover a wide range of azimuths and epicentral distances.

Given the encouraging results from the station coverage test, our next step is to consider whether certain source configurations bias retrieval. Previous documented examples of using ISOLA to resolve multiple sub-events assumed a fixed focal mechanism[4,5]. However, in this paper, our objective is to assess source complexity due to triggering on adjacent faults; therefore, we tested a combination of sub-event faulting types. Our four multiple point-source scenarios and corresponding results are summarised in Supplementary Figure 1 and Supplementary Table 3. For the majority of cases, the inversion resolves the timing of the two sub-events; the relative moment of the sources is also recovered. However, for single point-source inversions, the recovered moment release does not always equal the sum of both input sub-events. This discrepancy is particularly noticeable where both sub-events comprise a

combination of reverse faulting (Cases A and B), which also results in a lower variance reduction (VR). Importantly, apart from where the offshore sub-event is larger and/or ruptures earlier (Case D), the double-couple percentage (%DC) from the single-source inversion is quite high, potentially masking source complexity[6]. In this case, the retrieved mechanism is most similar to the first sub-event. We speculate that this discrepancy may come from the complex superposition of long period, high amplitude waves from these two events when they arrive at the stations. This result occurs due to the uneven distribution of stations. Therefore, we may not be able to resolve a doublet involving a larger offshore rupture occurring before a smaller earthquake that is situated closer to the stations.

Based on VR and sub-event retrieval performance, the best source configuration for our network coverage is the case of a thrust event followed by a smaller normal fault rupture located further offshore (Case C).

Relative uncertainty estimates

As a second synthetic test, we quantify the relative uncertainty in source mechanism caused by reduced azimuthal coverage on the inversion's capability to resolve sources located far offshore. Here, we generated 1-D synthetics for a range of single-source faulting types located offshore (Supplementary Table 3). We used a tool in ISOLA to calculate theoretical uncertainty in moment tensors caused by inaccurate Green's functions. Such an uncertainty estimate is relative because data variance is unknown. However, relative uncertainties can be calculated between two sets of station configurations. A 5D error ellipsoid is computed and a mean Kagan angle is given, providing an estimate of the error in focal mechanism parameters, with respect to an optimum solution. We computed focal mechanism uncertainties for two scenarios: one using the real station coverage (Fig. 1); the other using an optimal network with perfect azimuthal distribution. The results from this test are shown in Supplementary

Table 3. We found that errors using the actual, reduced station coverage are only 12–39% greater than those using an optimal network. Interestingly, the uncertainties are smaller when the focal mechanism has a nodal plane striking in the same direction as the network (north-west). These results therefore imply that we can trust the focal mechanisms of offshore seismic sources using our station distribution.

Supplementary Note 3: Statistical significance of adding a second point-source

In order to test the statistical validity of fitting the waveforms using the second sub-event, we assess the significance of the variance reduction using the *F* test. Similar tests have been previously carried out for multiple point-source moment tensor inversions[7,8]. Each model is characterised by the variance between synthetic and observed waveforms:

$$E = \sum [O_i - S_i]^2$$

where *O* and *S* represent the observed and synthetic data, respectively. We therefore define the ratio:

$$F = \frac{E(\text{model 2})}{E(\text{model 1})}$$

which is compared with the *F* test values at different confidence levels and for different degrees of freedom, *dof*., where $dof = N - M$. *N* corresponds to the number of data points and *M* is the number of free parameters (*M* = 5 for a deviatoric inversion). Data at low frequencies are clearly correlated, but we assume that the data are uncorrelated when the waveforms are sampled within the studied period range[9] (> 12 s based on our low-pass filter corner). Moment tensors are calculated over a time window that is 245.76 s in length (Fig. 2a). Using our low-pass filter corner frequency of 0.08 Hz, we are thus only able to resolve

minimum waveform periods of 19.7 s, which results in 655 data points for each component (sampling frequency of 33 Hz). For all three components and seven stations, we thus have a total of 13755 data points, resulting in 13750 degrees of freedom for a deviatoric moment tensor.

The variance ratio, F between our single and two-point-source moment tensor inversions equals 1.61, which is much greater than the critical F value of 1.28 at a confidence level of 99.95%. Therefore, we argue that the introduction of a second point-source is statistically significant with a very high confidence.

Supplementary Note 4: Relocation of and single source moment tensor inversion of aftershocks

A thorough analysis of aftershocks is needed because there are no available CMT solutions from the global agencies; the largest recorded aftershock had M_b 4.9 (based on the USGS-NEIC catalogue). We searched continuous waveforms from local onshore and OBS stations in the 30 days following the mainshock. To ensure robust locations, we only relocated events that had a minimum of five P-wave and three S-wave observations. The relocation was performed in a similar way to that of the mainshock (Supplementary Note 1). The average standard error in depth of our aftershock relocations is 1.2 km. We also inverted for single point-source moment tensor solutions of aftershocks in the frequency range 0.05–0.11 Hz. The grid search was carried out over a range of depths, centred on each hypocentre location. Centroid depths were generally very consistent with hypocentral depths. Solution quality was tested using different combinations of stations and velocity models, as well as crosschecking with first motion polarities.

Supplementary Note 5: Regional recordings of the Araucania earthquake from permanent GSN stations

We investigated whether the double-source configuration of the Araucania earthquake could be detected in regional and teleseismic waveforms. We compared the Araucania earthquake to other similar-sized aftershocks of the Maule sequence, the March 2012 M_w 7.1 Constitución and the March 2010 M_w 6.9 Pichilemu earthquakes. The GCMT solutions and detailed studies[10,11] of these earthquakes show that the former is a straightforward plate interface thrusting event, whereas the Pichilemu event occurred on a normal fault in the overriding plate. Therefore, we are able to directly compare a simple plate interface thrust and an upper plate event with a complex doublet involving both faulting styles.

We focussed our attention on the closest permanent GSN station that was operating for both earthquakes, TRQA, in Argentina, which is located roughly equidistant (8–9°) from all three earthquakes. Comparison of normalised power spectra for these three events (Supplementary Figure 8) reveals a greater proportion of high frequency energy from the Araucania and Pichilemu earthquakes, particularly in the frequency range 0.1–0.2 Hz. Therefore, we speculate that the partitioning of the Araucania rupture into the upper plate generates more high frequency energy compared to a single-source plate interface rupture. It is possible that higher frequency radiation is due to slip on immature upper plate faults, compared to the presumably more mature megathrust fault[12]. These characteristics may aid with the detection of similar plate interface - upper plate doublets in the future.

Supplementary Note 6: Calculations of seafloor displacement

Based on our knowledge of seismic velocity structure in the region of the Araucania earthquake[1,3] and scaling relationships of subduction zone earthquake fault dimensions[13], we calculated the expected seafloor static displacement from a rupture in the upper plate. This

Seismic slip on an upper plate normal fault during a large subduction megathrust rupture calculation was based on an approximation of dislocation faulting in a homogeneous half-space[14]. The very low S-wave velocities in the marine forearc (Supplementary Figure 5) correspond to a lower rigidity, and hence a greater slip for a given fault area and seismic moment.

For the size, depth and faulting mechanism of Event II (M_w 6.7) of the Araucania earthquake, we calculate a maximum vertical seafloor displacement of 0.3 m. If this faulting mechanism is scaled up to M_w 7.0, we find a vertical seafloor displacement of 0.7 m. Finally, if we assume an M_w 7.0 with pure normal faulting, we find that the vertical displacement increases to 1.2 m.

Supplementary Tables

	Origin time (UTC)	Longitude (°)	Latitude (°)	Depth (km)	Ref.
1-D relocated	20:20:1	-73.82	-38.47	39	*This study*
3-D relocated	20:20:15	-73.73	-38.54	23	
CSN (Chile)	20:20:11	-73.96	-38.34	18	[15]
USGS NEIC	20:20:17	-73.33	-38.36	24	[16]
GFZ-GEOFON	20:20.17	-72.33	-38.23	12	[17]

Supplementary Table 1: Hypocentral estimates for the Araucania earthquake.

	Centroid			Moment tensor				Ref.
	Longitude (°)	**Latitude (°)**	**Depth (km)**	**Nodal plane 1**	**Nodal plane 2**	**%DC**	M_w	
Regional CMT	-73.73	-38.54	23	345/18/71	184/73/96	89	7.0	*This study*
USGS NEIC (*w*-phase)	-73.35	-38.37	24	016/14/115	171/77/84	96	7.1	[16]
Global CMT	-73.84	-38.71	19	005/13/97	178/77/88	97	7.1	[18]

Supplementary Table 2: Single point-source CMT solutions for the Araucania earthquake. Nodal planes are described by strike/dip/rake (°).

Case	Input sources				Recovered sources											
	Sub-event I (t = 10 s)		Sub-event II (t = 20 s)		Single-source inversion				Multiple-source inversion							
									Sub-event I				Sub-event II			
	Pos.	Mech.	Pos.	Mech.	Pos.	Time (s)	Mech.	%DC	Pos.	Time (s)	Mech.	Rot. angle	Pos.	Time (s)	Mech.	Rot. angle
A	33	357/10/90	16	357/10/90	41	12	29/12/18	90	33	10	4/9/96	3	33	20	5/3/97	1
B	33	357/10/90	16	0/60/90	33	10	4/89/-97	97	33	10	351/8/86	3	16	20	1/59/90	1
C	33	357/10/90	16	0/60/-90	33	10	15/19/111	99	33	10	0/9/92	2	16	20	1/59/-89	1
D	16	0/60/-90	33	357/10/90	32	19	218/9/-49	72	1	4	178/39/-99	12	32	19	210/11/-61	21

Supplementary Table 3: Results from the synthetic sensitivity tests described in Supplementary Note 1 and presented in Supplementary Figure 1. Pos. = source position (as shown in Fig. 2); Mech. = focal mechanism; Rot. angle = rotation angle with respect to input source mechanism.

Input solution at source position 16 (strike/dip/rake)	**Focal mechanism uncertainty (mean Kagan angle [°])**		**% Error due to actual station configuration**
	Real station configuration	**Ideal station configuration**	
010/15/090 	4.48	3.91	15%
000/45/090 	4.84	3.81	26%
045/45/090 	4.25	3.79	12%
090/45/090 	5.22	3.78	38%
000/45/-090 	4.84	3.81	27%
312/45/-116 	5.30	3.97	34%
000/90/180 	5.32	3.86	38%
045/90/180 	5.38	3.88	39%

Supplementary Table 4: Relative uncertainty estimates of different faulting styles for a single point-source located offshore (source position 16). Uncertainties are calculated for both our actual station distribution (Fig. 1) and a network of ideally distributed stations.

	Centroid				Moment tensor			
	Time shift relative to origin	**Longitude (°)**	**Latitude (°)**	**Depth (km)**	**Nodal plane 1**	**Nodal plane 2**	**%DC**	M_w
Event I	10.9	-73.61	-38.42	26	181/81/90	356/9/84	98	6.8
Event II	23.2	-73.85	-38.66	19	329/44/-116	183/51/-66	89	6.7

Supplementary Table 5: Final two-point-source solutions for the Araucania earthquake based on this study, accounting for source location bias due to 3-D waveform effects. Nodal planes are described by strike/dip/rake (°).

Station removed	Event I					Event II				
	Time shift (s)	Source location	Nodal plane 1	M_w	Focal mech.	Time shift (s)	Source location	Nodal plane 1	M_w	Focal mech.
Optimum solution	10.9	33	356/9/84	6.8		23.7	16	312/45/-116	6.7	
QF26	13.8	39	303/19/29	6.8		23.7	16	317/39/-127	6.7	
QC05	10.9	33	351/3/86	6.8		23.7	16	320/43/-120	6.7	
L003	10.9	33	012/03/96	6.9		22.7	16	321/30/-127	6.8	
QC04	10.9	33	343/3/75	6.8		23.7	16	321/39/-120	6.7	
L101	10.9	33	323/3/47	6.9		23.7	16	316/40/-129	6.8	
QC02	10.9	33	325/3/86	6.8		23.7	16	320/39/-124	6.7	
QF25	10.9	33	334/3/61	6.8		22.7	16	320/32/-127	6.7	

Supplementary Table 6: Source stability of the multiple point-source solution based on the results of removing one station at a time from the inversion (jackknifing). These jackknifing results are compared with the optimum solution obtained using all available stations. Source location refers to the grid position illustrated in Fig. 2b. Stations are ordered in terms of epicentral distance. These results show the remarkably consistent mechanisms for both sub-events, indicating independence from the exact set stations used in the inversion.

	Event I					Event II				
	Source location	Time shift (s)	Nodal plane 1	M_w	Focal mech.	Source location	Time shift (s)	Nodal plane 1	M_w	Focal mech.
Optimum solution	33	10.9	356/9/084	6.8		16	23.7	312/45/-116	6.7	
Fixed locations for Event I	41	13.6	61/12/152	6.8		16	23.2	314/43/-133	6.7	
	34	11.8	48/16/134	6.8		16	23.2	312/43/-135	6.7	
	27	10.0	41/20/122	6.8		16	23.2	309/44/-137	6.7	
	26	8.8	9/13/092	6.8		16	23.2	310/43/-137	6.7	
	25	7.9	332/14/056	6.9		9	11.2	337/38/070	6.8	
	32	10.3	316/15/045	6.8		16	23.5	313/43/-133	6.7	
	39	12.7	306/14/038	6.8		16	23.2	314/42/-129	6.7	
	40	13.0	336/3/069	6.8		16	23.2	315/42/-133	6.7	

Supplementary Table 7: Dependence of Event II solution on the position and mechanism of Event I.

Supplementary Figures

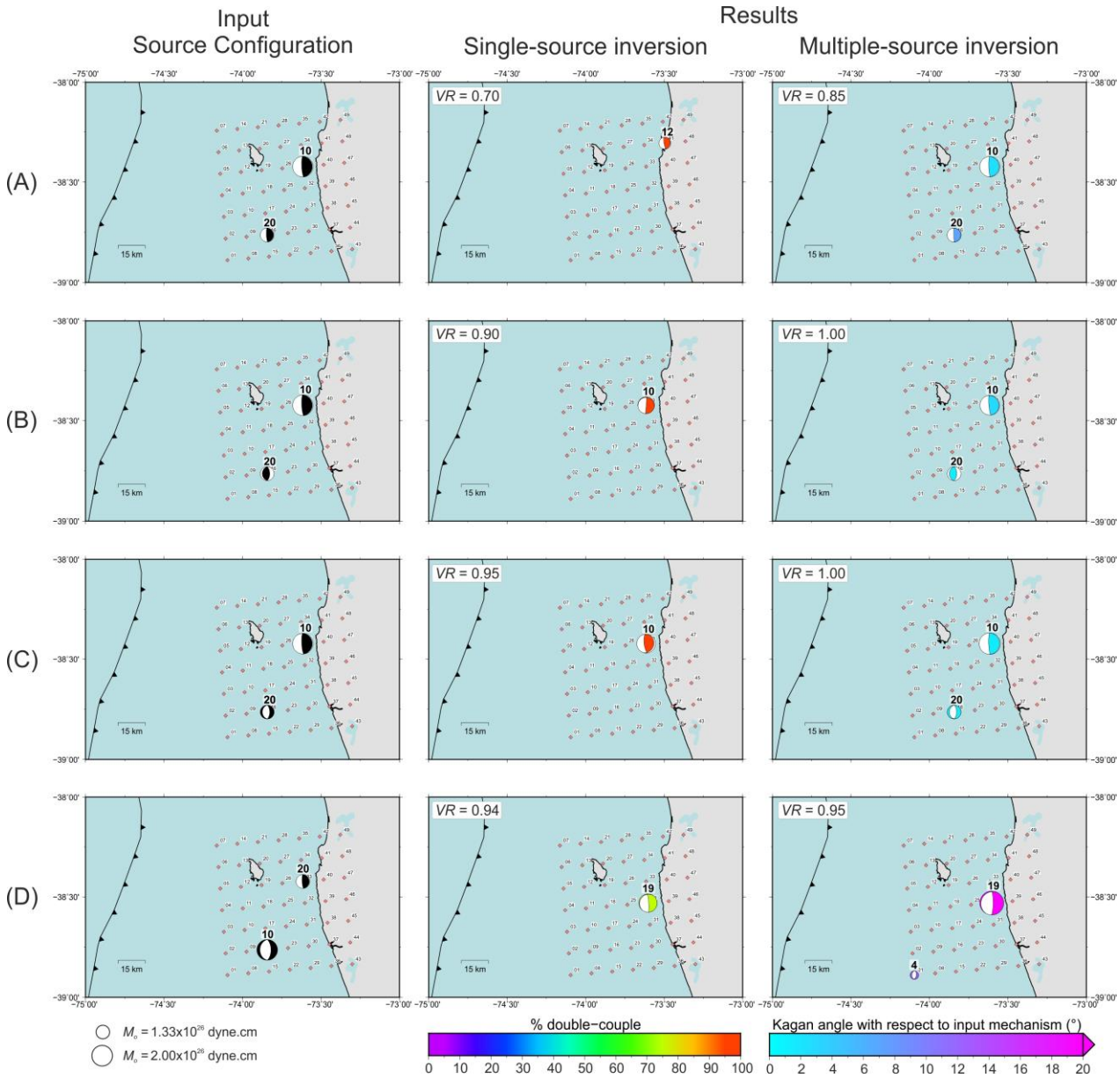

Supplementary Figure 1: Synthetic source recovery tests using simulated waveforms for different source configurations (A-D). The number above each beach ball represents the input and recovered centroid time of each source. For the inversion results, the number in the white box indicates the VR. For the single-source inversion, focal mechanisms are coloured by %DC. For the multiple source inversion results, focal mechanisms are coloured by the Kagan angle[19] (minimum rotation angle) with respect to the corresponding input mechanisms. These results are detailed in Supplementary Table 3.

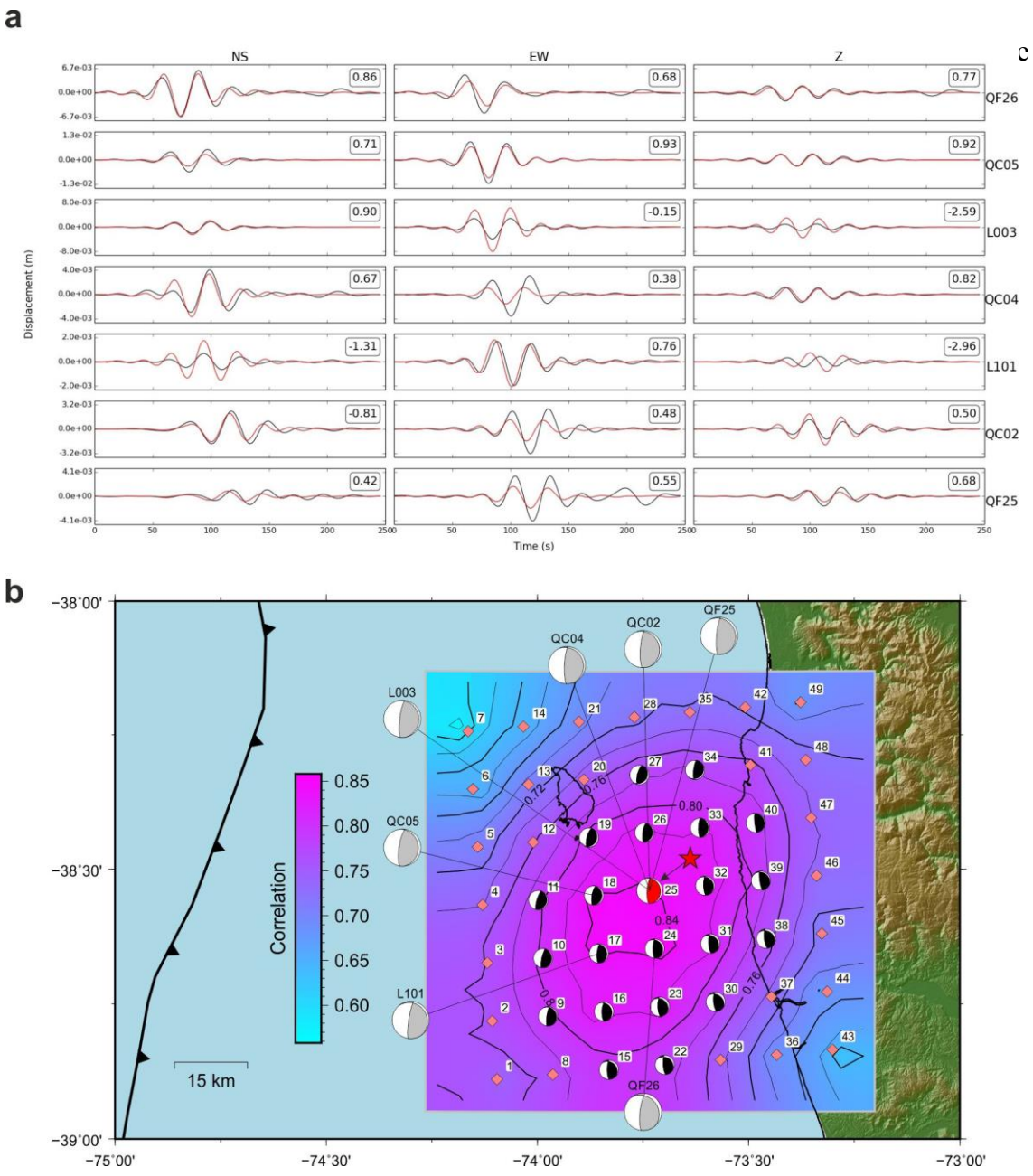

Supplementary Figure 2: Single source inversion results. a) Comparison between the observed (black) and synthetic (red) waveforms for the optimum solution. Waveforms are bandpass filtered in the frequency range 0.02–0.04 Hz. Station names are shown on the right and the components are labelled at the top. Numbers at next to waveforms denote the corresponding variance reduction. b) Grey beach balls show solution variability based on station jackknifing tests, labelled with the station removed in each inversion. The coloured grid represents the correlation between observed and synthetic records as a function of trial single-source position (numbered). Solutions that lie within 90% of the optimum solution's VR are plotted as black beach balls. The solution with the highest correlation is plotted in red. The final solution has a high %DC of 89%. The red star denotes the earthquake's epicentre.

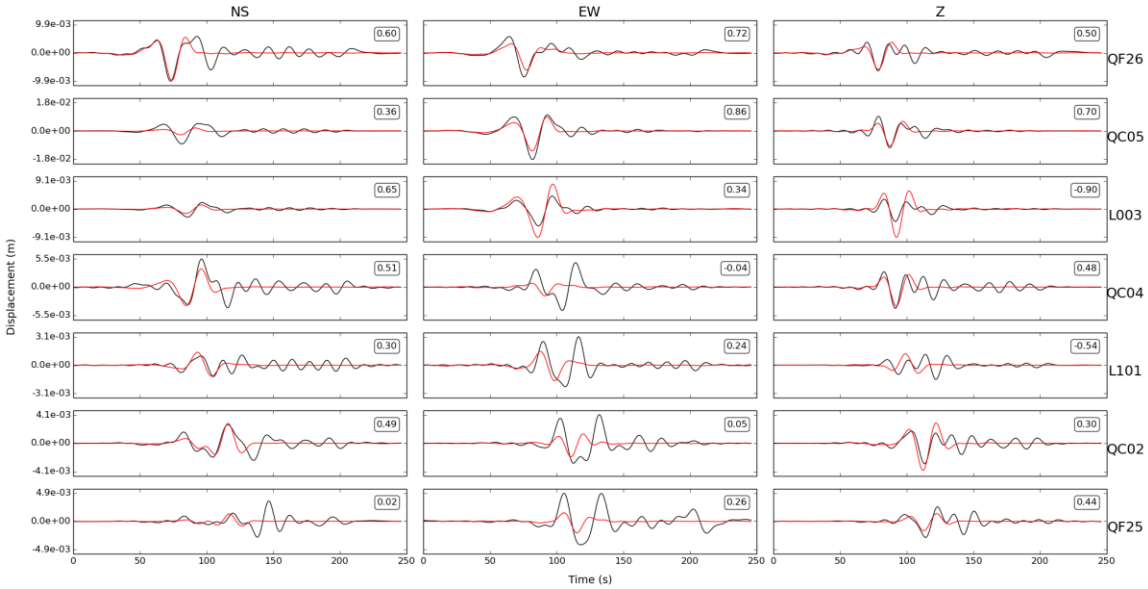

Supplementary Figure 3: Comparison between the observed (black) and synthetic (red) waveforms at high frequencies (0.02–0.08 Hz) solution using a single point-source. Station names are labelled. Numbers alongside each waveform component denote the corresponding VR.

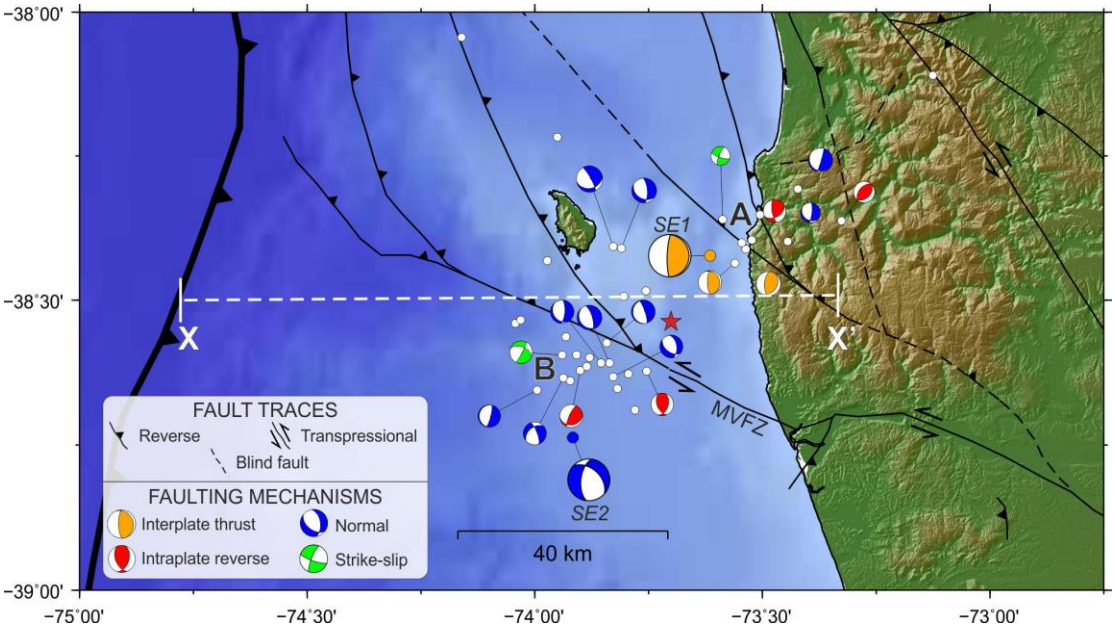

Supplementary Figure 4: Map showing the locations and focal mechanisms of aftershocks and mainshock events (as for Fig. 3). In this case, the location of Event II is based on the raw 1-D iterative deconvolution multiple point-source solution, and not corrected for 3-D waveform effects.

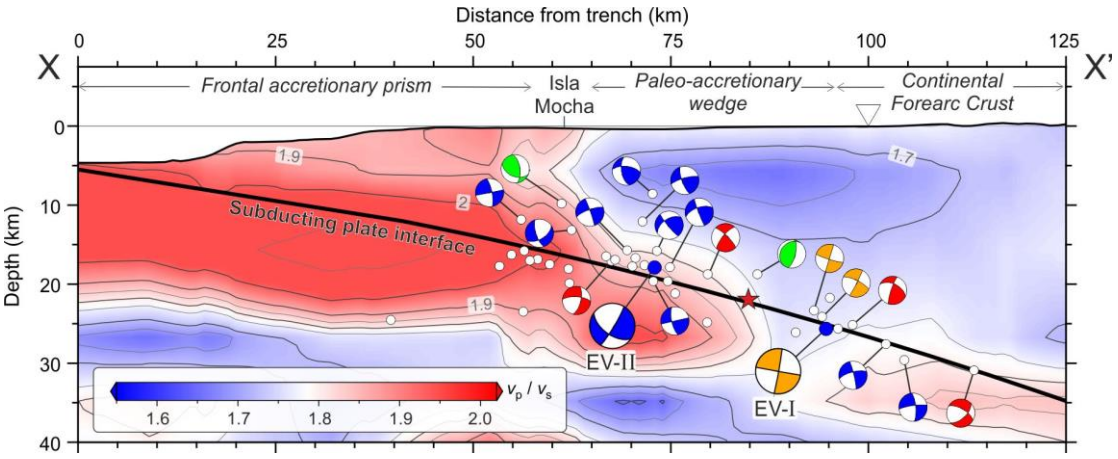

Supplementary Figure 5: Cross-section showing the locations and focal mechanisms of aftershocks and mainshock events (as for Fig. 3b) plotted on top of v_p/v_s ratio[1,3].

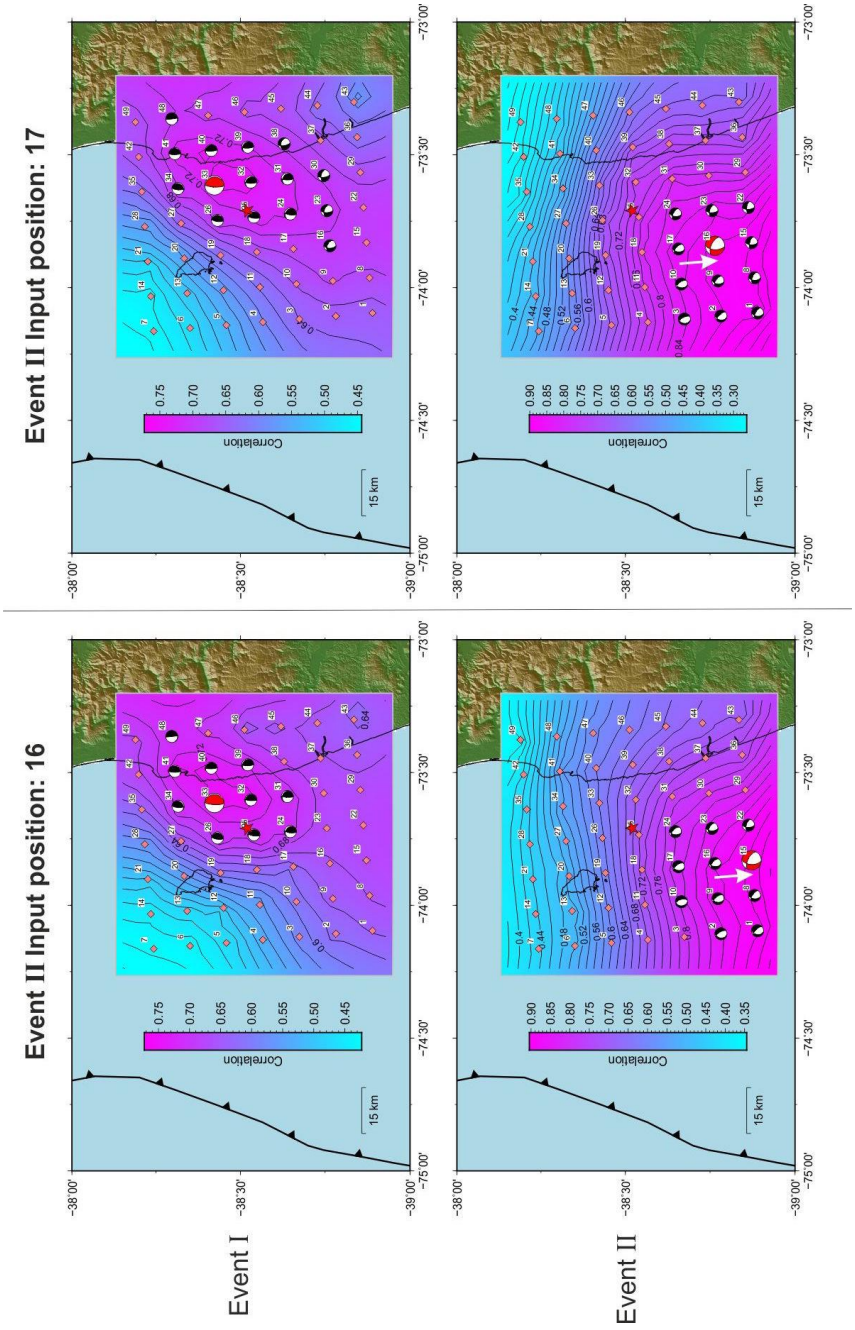

Supplementary Figure 6: Recovery of 3-D synthetic waveforms using the inversion method based on 1-D Greens functions. In each case, input sources are based on the result from our real data inversion. On the right, the source position of Event II is placed at source position 17. In each case, the 1-D inversion results in a systematic southward shift, as shown by the arrows.

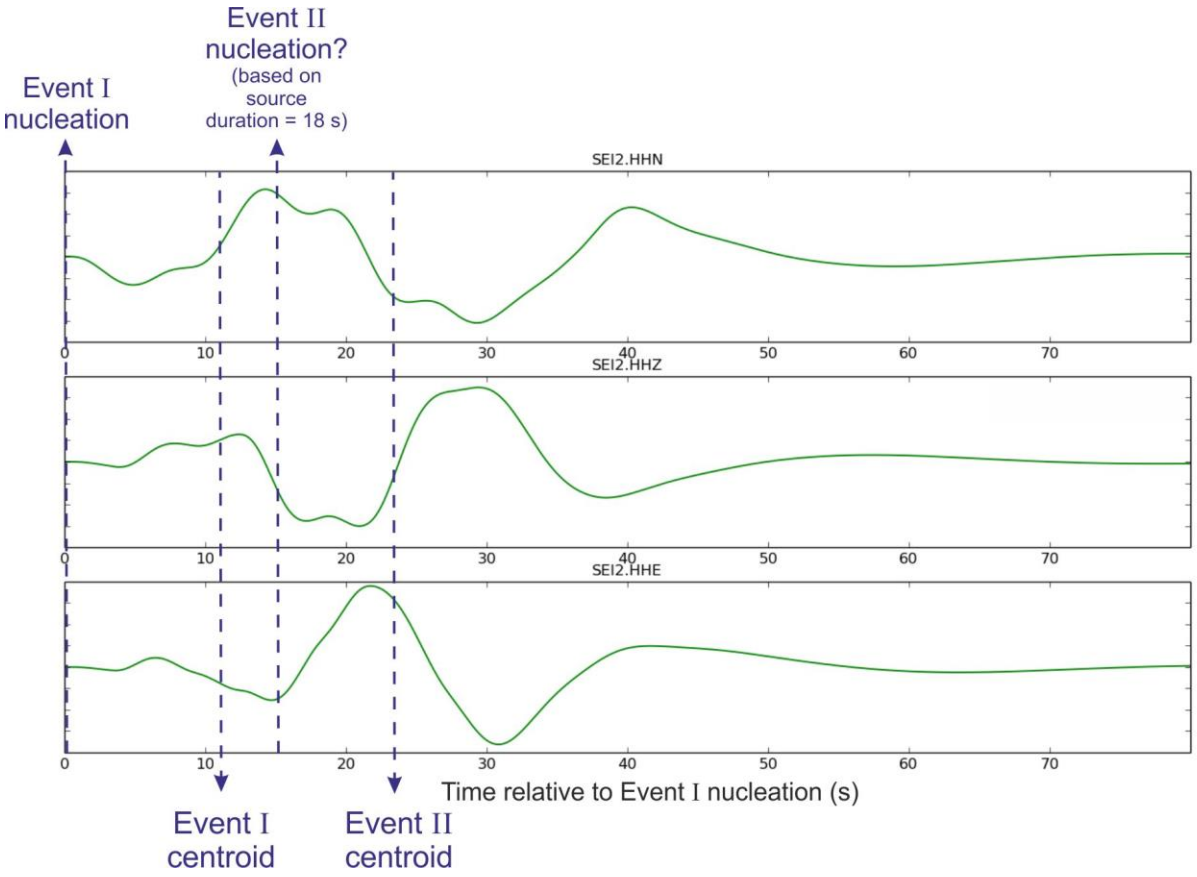

Supplementary Figure 7: Three-component velocity traces of the simulated seismic wavefield of Event I 'seen' by Event II. The waveform is bandpass filtered at 0.02–0.15 Hz. The 3-D simulation is generated in the same way as described in the main text; in this case, a receiver is placed at the centroid location of Event II. The known centroid times of Events I and II are shown. Although we cannot pinpoint the exact nucleation time of Event II, it is clear that the arrival of high amplitude S-waves from Event I is coincident with the possible nucleation stage of Event II, based on its source duration of 18 s.

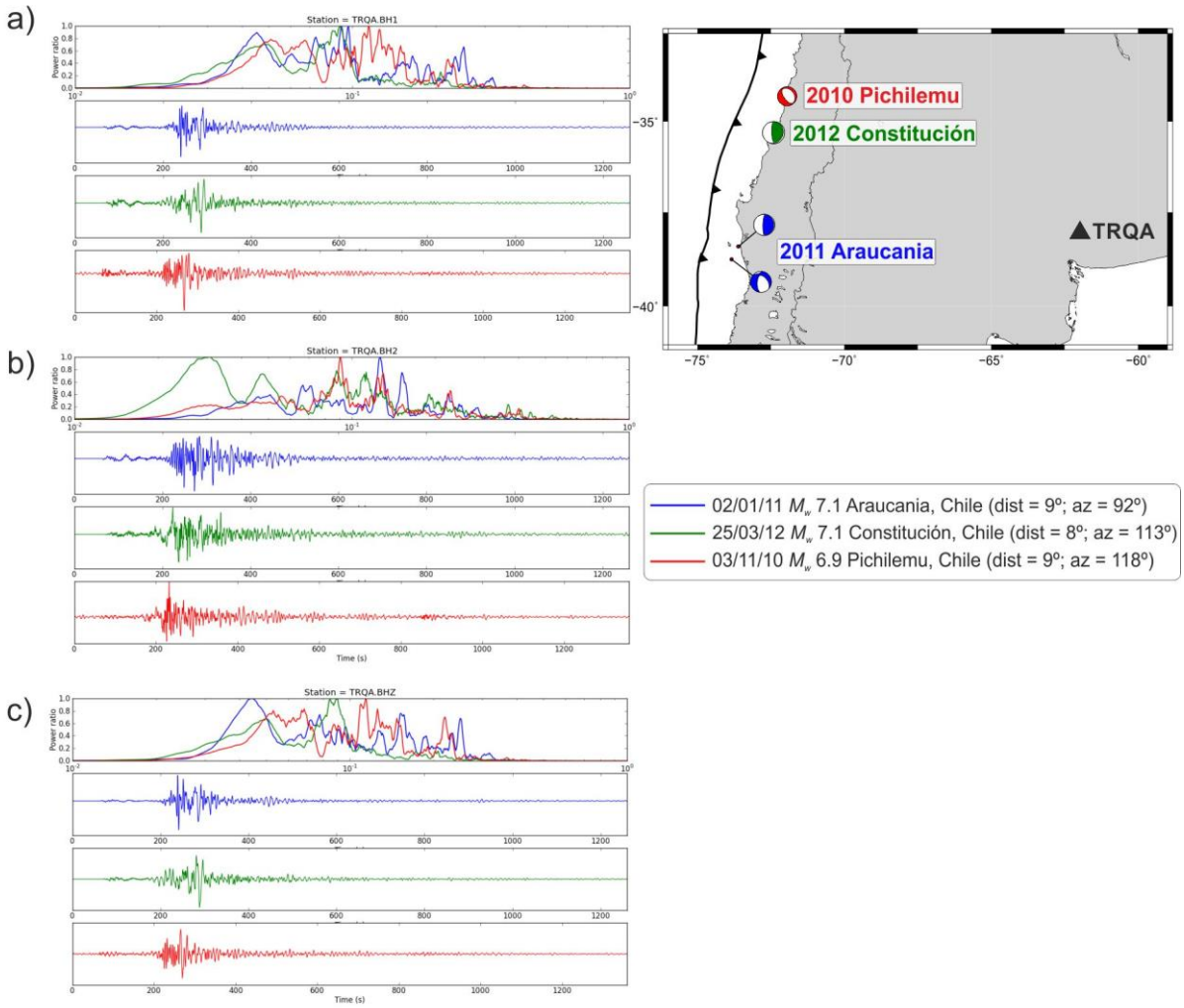

Supplementary Figure 8: Regional recordings of the M_w 7.1 2011 Araucania (plate interface thrusting and upper plate normal faulting), 2012 M_w 7.1 Constitución (plate interface thrusting only) and 2010 M_w 7.1 Pichilemu (upper plate normal faulting only) earthquakes at the permanent GSN station, TRQA in eastern Argentina. The left hand panel shows the normalised frequency (top) spectra and traces for each component: a) west; b) east; c) vertical. The map in the right-hand panel shows the location of the three earthquakes, corresponding CMT solutions and the location of station TRQA.

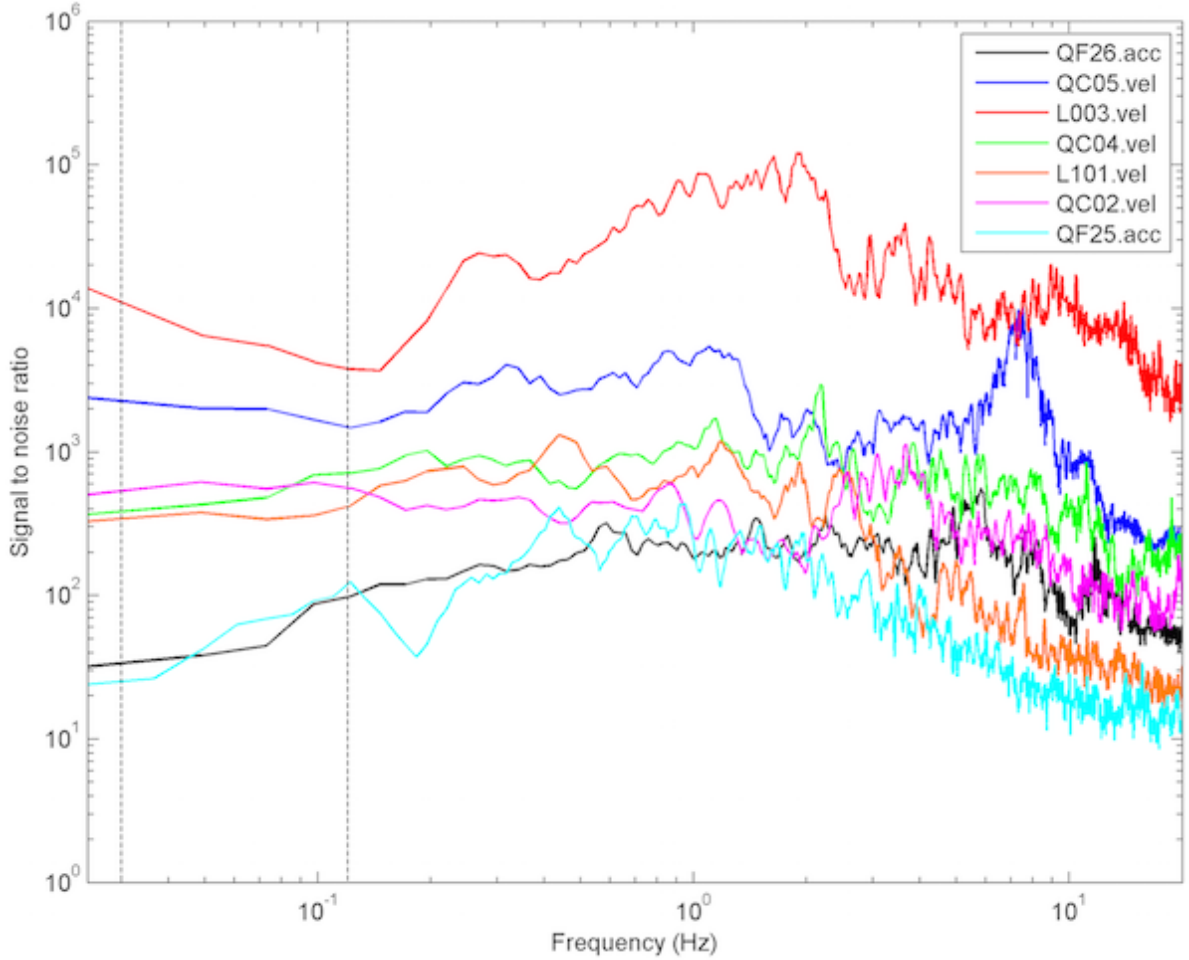

Supplementary Figure 9: Signal-to-noise ratio analysis for stations used in the single- and multiple point-source inversions. The dashed vertical lines denote the approximate frequency range used in this study.

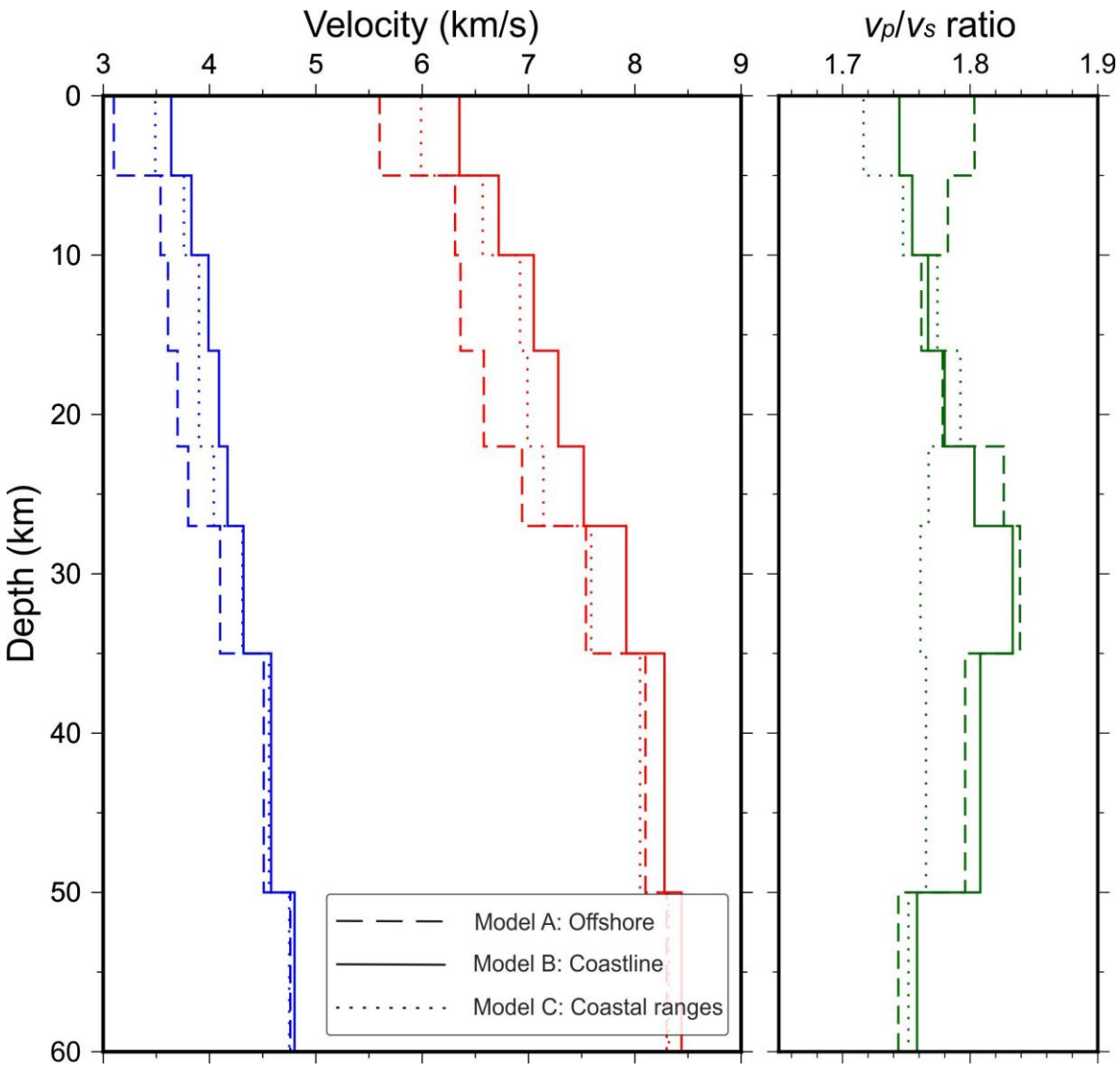

Supplementary Figure 10: 1-D velocity models tested in this study based on local tomographic models[1,3]. Model B (Coastline) was used as the optimum 1-D velocity model to generate the final source solutions in this study.

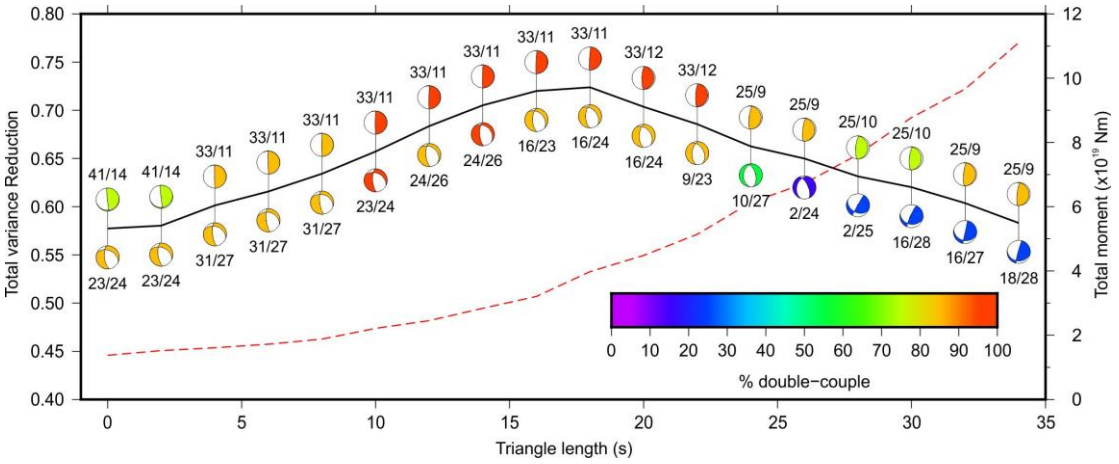

Supplementary Figure 11: Correlation (black line) and total moment (red dashed line) of the multiple point-source solution as a function of triangle source length for the high frequency, multiple point-source inversion using iterative deconvolution. The beach balls above and below the line give the corresponding mechanism for Events I and II, respectively.

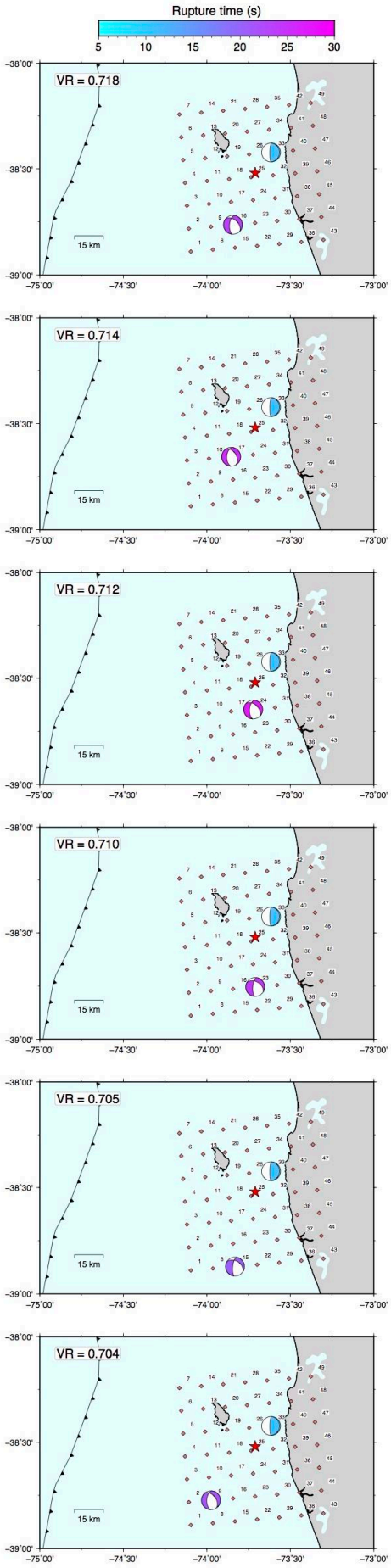

Supplementary Figure 12: Best-fitting solutions (within the 98th percentile) for the two-point-source, high-frequency solution using the constrained non-negative least squares method. The colour of each beach ball indicates the centroid time of each source.

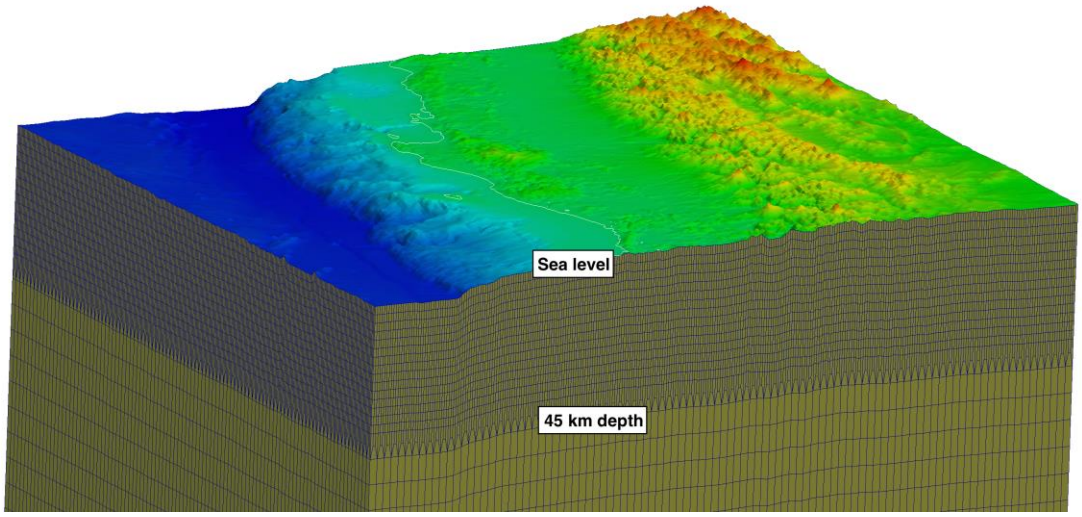

Supplementary Figure 13: 3-D view of the hexahedral mesh used for the 3-D waveform simulations. This mesh honours surface relief and bathymetry, but does not contain dipping geological discontinuities at depth.

Supplementary References

1. Hicks, S. P., Rietbrock, A., Ryder, I. M. A., Lee, C.-S. & Miller, M. Anatomy of a megathrust: The 2010 M8.8 Maule, Chile earthquake rupture zone imaged using seismic tomography. *Earth Planet. Sci. Lett.* **405,** 142–155 (2014).
2. Hayes, G. P., Wald, D. J. & Johnson, R. L. Slab1. 0: A three- dimensional model of global subduction zone geometries. *J. Geophys. Res.* **117,** (2012).
3. Haberland, C., Rietbrock, A., Lange, D., Bataille, K. & Dahm, T. Structure of the seismogenic zone of the southcentral Chilean margin revealed by local earthquake traveltime tomography. *J. Geophys. Res.* **114,** B01317 (2009).
4. Zahradnik, J. & Sokos, E. The Mw 7.1 Van, Eastern Turkey, earthquake 2011: two-point source modelling by iterative deconvolution and non-negative least squares. *Geophys. J. Int.* **196,** 522–538 (2014).
5. Quintero, R., Zahradnik, J. & Sokos, E. Near-regional CMT and multiple-point source solution of the September 5, 2012, Nicoya, Costa Rica Mw 7.6 (GCMT) earthquake. *J. S. Am. Earth Sci.* **55,** 155–165 (2014).
6. Rivera, L. & Kanamori, H. Diagnosing Source Geometrical Complexity of Large Earthquakes. *Pure. Appl. Geophys.* **171,** 2819–2840 (2014).
7. Adamova, P., Sokos, E. & Zahradnik, J. Problematic non-double-couple mechanism of the 2002 Amfilochia Mw5 earthquake, Western Greece. *J Seismol* **13,** 1–12 (2008).
8. Sipkin, S. A. Interpretation of non- double- couple earthquake mechanisms derived from moment tensor inversion. *J. Geophys. Res.* **91,** 531–547 (1986).
9. Dreger, D. & Woods, B. Regional distance seismic moment tensors of nuclear explosions. *Tectonophysics* **356,** 139–156 (2002).
10. Ruiz, S. *et al*. The Constitución earthquake of 25 March 2012: A large aftershock of the Maule earthquake near the bottom of the seismogenic zone. *Earth Planet. Sci. Lett.* (2013). doi:10.1016/j.epsl.2013.07.017
11. Ryder, I. *et al*. Large extensional aftershocks in the continental forearc triggered by the 2010 Maule earthquake, Chile. *Geophys. J. Int.* **188,** 879–890 (2012).
12. Choy, G. L., McGarr, A., Kirby, S. H. & Boatwright, J. *An Overview of the Global Variability in Radiated Energy and Apparent Stress. Subduction Top to Bottom* **170,** 43–57 (American Geophysical Union).
13. Blaser, L., Krüger, F., Ohrnberger, M. & Scherbaum, F. Scaling Relations of Earthquake Source Parameter Estimates with Special Focus on Subduction Environment. *B. Seismol. Soc. Am.* **100,** 2914–2926 (2010).
14. Okada, Y. Internal deformation due to shear and tensile faults in a half-space. *B. Seismol. Soc. Am.* **82,** 1018–1040 (1992).
15. Centro Sismológico Nacional. Centro Sismológico Nacional, Universidad de Chile. (2011). at <http://www.sismologia.cl>
16. United States Geological Survey National Earthquake Information Center. M7.2 - Araucania, Chile. (2011). at <http://earthquake.usgs.gov/earthquakes/eventpage/usp000hsfq#scientific_tensor>
17. Helmholtz-Zentrum - Potsdam Deutsches GeoForschungsZentrum (GFZ). GEOFON

Program GFZ Potsdam :: gfz2011adjs. (2011). at <http://geofon.gfz-potsdam.de/eqinfo/event.php?id=gfz2011adjs>

18. Ekström, G., Nettles, M. & Dziewoński, A. M. The global CMT project 2004–2010: Centroid-moment tensors for 13,017 earthquakes. *Phys*. *Earth*. *Planet*. *Inter*. **200-201,** 1–9 (2012).
19. Kagan, Y. Y. 3-D rotation of double-couple earthquake sources. *Geophys*. *J*. *Int*. **106,** 709–716 (1991).